Developing Superhydrophobic Copper-Graphene Nanoplatelet Coatings to Promote Dropwise Condensation Using Thermal Spray Techniques

Tahmineh Forati

A Thesis
In the Department
Of
Mechanical, Industrial and Aerospace Engineering

Montreal, Quebec, Canada

Presented in Partial Fulfillment of the Requirements
For the Degree of
Master of Applied Science (Mechanical Engineering) at
Concordia University
Montreal, Quebec, Canada

CONCORDIA UNIVERSITY

School of Graduate Studies

This is to certify that the thesis prepared

By: Tahmineh Forati

Entitled: Developing Superhydrophobic Copper-Graphene Nanoplatelet Coatings to Promote Dropwise Condensation Using Thermal Spray Techniques

And submitted in partial fulfilment of the requirements for the degree of

Master of Applied Science (Mechanical Engineering)

Complies with the regulations of the University and meets the accepted standards with respect to originality and quality.

Signed by the final Examining Committee:

_____ Chair
Dr. Muthu Packirisamy

_____ External Examiner
Dr. Saifur Rahaman

_____ External to Program

_____ Examiner
Dr. Rolf Wuthrich

_____ Examiner

_____ Thesis Co-Supervisor
Dr. Martin Pugh

_____ Thesis Co-Supervisor
Dr. Christian Moreau

_____ Thesis Co-Supervisor
Dr. Ali Dolatabadi

Approved by: _____
Chair of Department or Graduate Program Director

_____ 2019_____ Dean of Faculty

Abstract

Developing Superhydrophobic Copper-Graphene Nanoplatelet Coatings to Promote Dropwise Condensation Using Thermal Spray Processes

Tahmineh Forati

Concordia University, 2019

Water vapour condensation is frequently used as an effective means of transferring heat using dropwise condensation on non-wetting surfaces. The rate of heat transfer can be enhanced with dropwise condensation on non-wetting or hydrophobic surfaces when compared to filmwise condensation on a wetting surface. A potential method to improve dropwise condensation is the use of superhydrophobic coatings that are exceptionally water repelling. The superhydrophobicity of a surface is a result of the combination of its surface microstructure and surface chemistry. Materials with low surface energy are mostly polymeric and organic with low durability and poor thermal and chemical stability. Furthermore, these materials add thermal resistance to the coating, limiting the potential heat transfer capacity. As an alternative, developing a coating containing graphene nanoplatelets (GNP) with their hydrophobicity, high thermal conductivity and excellent mechanical properties is a promising approach to provide a hydrophobic coating for promoting dropwise condensation.

In order to develop micro-textured coatings with high water repellency and mobility, in this work, atmospheric plasma spray (APS) and high-velocity oxy-fuel (HVOF) techniques were used as scalable and efficient coating techniques to develop thin Cu-GNP coatings on a copper substrate. The main reason for combining copper with GNP is to protect the GNP against the elevated temperatures of the plasma and HVOF plumes. Additionally, copper can act as a carrier which transfers the GNP towards the substrate hence the adhesion and mechanical properties of this coating improve as the substrate of interest is also copper. A parametric study approach was used to optimize the APS and HVOF process parameters in order to achieve the best wettability in the copper/graphene nanoplatelets micro-textured coatings. Subsequently, to lower their surface energy, post-treatment by a stearic acid solution was performed.

The APS Cu-GNP coatings exhibit water contact angles as high as 152° and sliding angle less than10° while HVOF Cu-GNP coatings showed great water mobility (with a sliding angle less

than 1°) as well as high water contact angle value of 164°. The image analyses of the APS coatings showed a lamellar structure. Additionally, with optimizing the plasma power, the desired microstructure that encourages the non-wetting surface was achieved. The HVOF coating showed more homogenous as well as denser morphology, and a hierarchical microstructure was observed. With optimizing the parameters, GNP embedded in the Cu matrix was more evident in HVOF coatings which can be attributed to the lower temperature of this process. Raman analysis further demonstrates the presence of GNP in the coating while the defects in its structure increased after the thermal spray processes. Moreover, the above influences are more significant in APS compared to the HVOF Process. The best of the APS and HVOF coatings are then tested to evaluate their corrosion stability. It is shown that the HVOF Cu-GNP coating developed in this work can improve the corrosion resistance up to 89% when compared to the uncoated Cu surface. This coating can potentially promote dropwise condensation while offering enhanced corrosion stability.

Acknowledgement

My sincere gratitude and appreciation to my supervisors, Professor Ali Dolatabadi, Professor Christian Moreau and Professor Martin Pugh for the opportunity of performing this research in an exciting field of studies. Also, I would like to appreciate their continuous guidance, patience, encouragement and support during these years of my study.

I am grateful to Professor Rolf Wuthrich and Professor Mamoun Medraj from Concordia University for giving me permission to use their research facilities in their laboratories.

I wish to thank the entire Concordia University Thermal Spray Laboratory group members for all the help and encouragement during my work. Special thanks to Dr. Fadhel Ben Ettouil and Dr. Navid Sharifi, Hani Jazaerli and Alexandre Nascimento Romão for all the technical help during my experimental work. I would like also appreciate Hediyeh and Morvarid for their support during these challenging period. Thank you for being such a great and helpful team.

I extend my appreciation to Nanoxplore Inc. and Mitacs for financial support of the project also Tatiana and Nima for their help during my internship.

Also, all my gratefulness to my family and my boyfriend Ercan, for their unconditional love and support. Without them, this achievement would not have been possible.

Table of Contents

List of Figures

List of Tables

List of Abbreviations

Abbreviation	*Meaning (unit)*
ACA	Advancing Contact Angle (°)
APS	Atmospheric Plasma Spray
CAH	Contact Angle Hysteresis (°)
CLSM	Confocal Laser Scanning Microscopy
CR	Corrosion Rate
CVD	Chemical Vapor Deposition
DwC	Dropwise Condensation
FDO	perfluorododecylate
FwC	Filmwise Condensation
GNP	Graphene Nanoplatelets
GNR	Graphene Nanoribbons
GO	Graphene Oxide
HA	Hydroxyapatite
HTC	Heat Transfer Coefficient
HVOF	High-Velocity Oxygen Fuel
RCA	Receding Contact Angle (°)
SA	Sliding Angle (°)
SD	Standard Deviation
SEM	Scanning Electron Microscopy
WCA	Water Contact Angle (°)

List of Symbols

Symbol	Meaning (unit)
D_{10}	10% of particles are this particles size
D_{50}	50% of particles are this particles size
D_{90}	90% of particles are this particles size
R_a	Arithmetic mean height of the surface on a line
R_z	Maximum height of the surface on a line
S_a	Average surface area
γ_{LA}	Liquid/air interfacial energy
γ_{SA}	Solid/air interfacial energy
γ_{SL}	Solid/liquid interfacial energy
θ_0	Intrinsic water contact angle on an ideally smooth surface
θ_A	Advancing contact angle (°)
θ_C	Apparent contact angle of a rough surface (°)
θ_R	Receding contact angle (°)
θ_S	Sliding angle (°)
I_D/I_G	The ratio of D and G band intensities
Icorr	Corrosion current density
Ecorr	Corrosion potential
η	Corrosion resistance efficiency

Chapter 1. Introduction

1.1. Background and motivation

Condensation is a multiscale and multiphase phenomenon in nature, and it has numerous applications in industry. Surface engineering can lead to an enhancement in the efficiency of the condensation process which in turn can be involved in producing a profound environmental impact. Coatings play a primary role in improving surface properties such as corrosion resistance, hydrophobicity, and thermal resistance.

Graphene, a recently discovered carbon allotrope, has attracted worldwide attention and has been studied in different contexts due to its extraordinary properties and potential for innovative coatings. Some potential applications of graphene have been suggested by researchers, one of which is the promotion of dropwise condensation in industrial heat exchangers. Dropwise condensation is typically achieved by functionalizing the condenser surface with a hydrophobic coating. In a research study by Peterson et al. [1] graphene coatings were deposited to promote dropwise condensation by chemical vapour deposition (CVD). The results showed an efficiency improvement while offering robust chemical stability and maintaining low thermal resistance. Heat transfer enhancements by a factor 4 were demonstrated compared to film-wise condensation. Also, the robustness of these coatings was better than typical hydrophobic monolayer coatings.

In another study, Kim et al. [2] showed that graphene films could improve water-harvesting on surfaces while maintaining the intrinsic hydrophobicity of the surface. Moreover, graphene displays outstanding corrosion resistance and shows hydrophobic behaviour, while its inert chemical nature and mechanical strength indicate that it will resist degradation under typical condenser conditions. Corrosion is one of the leading industrial problems with an approximate annual cost of $2.2 trillion US [3]. Graphene with anti-corrosion properties can be an alternative material for advanced corrosion protection.

1.2. Current state of the art surface modification techniques

Several methods and various techniques have been employed to produce a surface to improve dropwise condensation and consequently heat transfer. The phase change on a solid surface is influenced by the energy and texture of the surface. Surface machining and roughening are examples of the techniques used to enhance the phase change heat transfer by increasing the net contact area for heat transfer and the number of nucleation or precipitation sites [4].

Coatings play an essential role in improving surface quality and can be used as a protection for a substrate. Several efforts have been made to improve coating properties including the surface properties of a substrate. As an example, wettability, corrosion resistance and adhesion can be mentioned. Numerous factors affect the resistance of a coating against potential destructive causes, namely the quality of the coating, the substrate characteristics, the properties of the coating-substrate interface and the corrosiveness of the environment. The surface structures achieved by surface machining and roughening are relatively simple. However, the coating can be more complicated in geometry and more versatile in material selection [5].

A significant potential method to improve dropwise condensation is the use of superhydrophobic coatings that are exceptionally water repelling. On superhydrophobic surfaces condensate droplets can rapidly be removed from the surfaces due to the slight adhesion between droplets and the substrates; consequently, new spots on the surface are repeatedley exposed to a condensation process. As a result, dropwise condensation avoids the accumulation of a thick condensate liquid film on the substrate that would significantly reduce the rate of heat transfer [6].

The superhydrophobicity of a surface can be achieved by the combination of the surface micro-texture and surface energy. Using superhydrophobic coatings is very challenging since the low-surface-energy materials are mostly organic and polymeric and their poor durability and chemical stability are serious concerns. Furthermore, regarding the nature of these coatings, any potential heat transfer enhancement is of limited effect since these coatings have originally low thermal conductivity [7].

1.3. Objectives

In order to develop and enhance surface properties for dropwise condensation the objectives of the current study can be summarized as follows:

- Development of Cu/GNPs coatings with low wettability and improved corrosion resistance using thermal spray techniques
- Optimization of the thermal spray coating conditions for Cu-GNP deposition to improve hydrophobicity

1.4. Thesis outlines

This work was performed with the goal of developing superhydrophobic copper-graphene nanoplatelet coatings for applications in heat transfer using thermal spray. This thesis is divided into five chapters. A brief description of the chapters are as follows:

Chapter 1 presents the backgrounds and motivations to develop this work. State of the art techniques to modify the surfaces are explained. The objectives and the scope of the work are explained as well as this thesis is outlined.

Chapter 2 reviews the literature related to this work. First, condensation is explained followed by the presentation of the wetting phenomena and superhydrophobicity. Finally, graphene-based coatings are described, followed by some researches performed on this topic. The last section of Chapter 2 highlights some of the coating processes.

In Chapter 3, the experimental procedure is discussed. Moreover, the experimental part of the work is detailed in this chapter.

Chapter 4 presents the results obtained and the findings are discussed. The coating characterization and the data extracted are presented, and further observations are performed. As a final point, the conclusions of the work and future research are specified in Chapter 5.

Chapter 2. Literature Review

This chapter will describe condensation, wetting phenomena and superhydrophobicity. Additionally, the graphene-based coatings and their methods of manufacturing will be presented. Last but not least, the different coating procedures will be explained.

2.1. Condensation

In engineering applications, condensation is considered as the phase change of a metastable vapour into a stable liquid. When the affinity between the condensing liquid and the solid surface is high, droplets of condensate form on the cooled substrate. The droplets grow by either continuous condensation followed by a continuous cooling or impact and coalescence during the sliding of drops.

2.1.1. Dropwise condensation

Dropwise condensation (DwC) occurs when condensation happens on a non-wetting surface. In most technical applications, the condensate is water which tends to wet metal surfaces, and eventually, filmwise condensation (FwC) takes place. Frequently, DwC appears on low-energy surfaces [4]. Heat transfer occurs from the gas phase to the substrate by the condensing droplets (except the direct heat transfer at the areas not covered by droplets). In DwC, advanced coalescence exposes some areas on the substrate for additional nucleation and growth [8].

Surface heat transfer coefficients (HTC) related to dropwise condensation are considerably larger than in the film condensation mode that takes place when the surface is wet. Dropwise condensation has been the target of attention during the past few decades. Heat transfer coefficients were reported to be 5 to 7 times higher than that of filmwise condensation. Hence, DwC

technologies should effectively aim at eliminating the droplets from the surface before their growth [9].

Film condensation, which is the formation of a thick film on the surface, occurs when the solid surface removes less condensate than is condensing on the surface. A condensing surface covered by the liquid film in this mode has a significant thermal resistance. Consequently, filmwise condensation exhibits lower HTC's than DwC; therefore, the design of substrates that promote heterogeneous nucleation is an obvious issue limited to condensation on solid substrates. Surface wettability has a profound impact on this aspect [4].

2.2. Wetting phenomena and superhydrophobicity

Wettability is defined by the contact angles of a drop resting on the surface. The interactions of a solid surface with water is usually characterized by its static water contact angle. The wetting behaviour of a surface depends on its surface chemistry and surface morphology [10].

2.2.1. Static water contact angle

The contact angle, described as a function of the interfacial tensions, is the angle between solid/liquid, solid/gas and liquid/gas interfaces. The water contact angle of a perfectly smooth surface, determined by θ_0, is the equilibrium contact angle that a water drop makes with the surface as demonstrated in Eq. (2.1), Young's equation

$$\cos\theta_0 = \frac{\gamma_{SV}-\gamma_{SL}}{\gamma_{LV}} \qquad \text{Eq. (2.1)}$$

Where γ_{SL}, γ_{SV}, and γ_{LV} are interfacial tensions between solid/liquid, solid/gas and liquid/gas, respectively [11]. Figure 2-1 represents a schematic of a drop on a surface describing interfacial tensions as forces that are in equilibrium. According to Young's equation when γ_{SV} is larger than γ_{SL}, i.e. the contact angle is less than 90°, the droplet tends to spread across the surface. This material is called hydrophilic and tends to get wet. In contrast, when γ_{SL} is larger than γ_{SV}, the contact angle is more than 90°; therefore, the surface tends not to get wet by water, and these materials are referred to as hydrophobic.

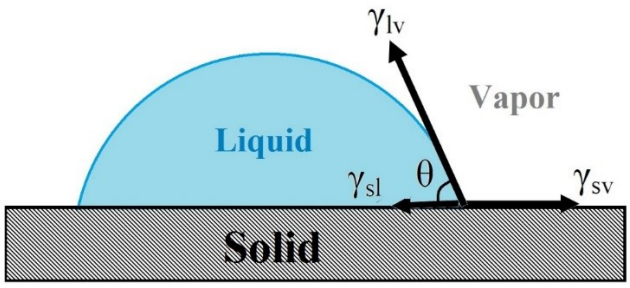

Figure 2-1. Schematic of a droplet on a surface showing the static contact angle

2.2.2. Water droplet mobility on a solid surface

Other parameters that determine the interaction of a moving water droplet on a solid surface are advancing contact angle (θ_A), receding contact angle (θ_R), and sliding angle (θ_S) presented in Figure 2-2.

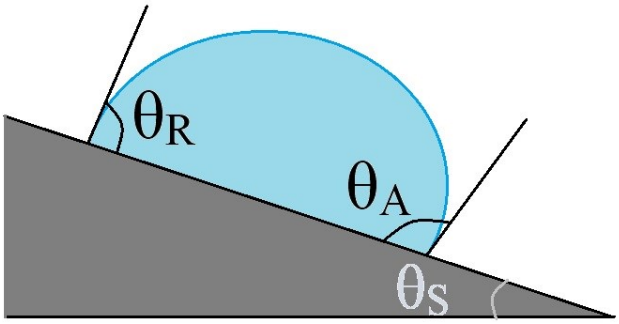

Figure 2-2. Schematic of sliding angle, advancing and receding contact angles of a drop on a tilted surface

Once water droplets start to move over a surface, the contact angle signified as θ_A on the front of the moving droplet is called the advancing contact angle (ACA) whilst the contact angle on the backward side of the droplet is called the receding contact angle (RCA), signified as θ_R. The difference among the receding and advancing angle results in the contact angle hysteresis. A surface with a small contact angle hysteresis tends to repel water [12]. Besides the mentioned parameters, the sliding angle which is the angle to which a surface needs to be tilted for a water droplet to move on that surface is used to characterize the surface properties. The lower the value of these two parameters, the higher the mobility the droplet will have on the surface [13].

2.2.3. Superhydrophobicity

Superhydrophobic surfaces that are exceptionally water-repellent have contact angles greater than 150°. Low water contact angle hysteresis or a sliding angle smaller than 10°, which allow water droplets on the surface to roll-off, are also defined as superhydrophobic characteristics [14]. The lotus leaf is a famous example of a superhydrophobic surface in nature due to its hierarchical surface roughness [15]. Scanning Electron Microscope (SEM) imaging of the surface of a lotus leaf in Figure 2-3 at two different magnifications shows the "hierarchical" microstructure on the surface.

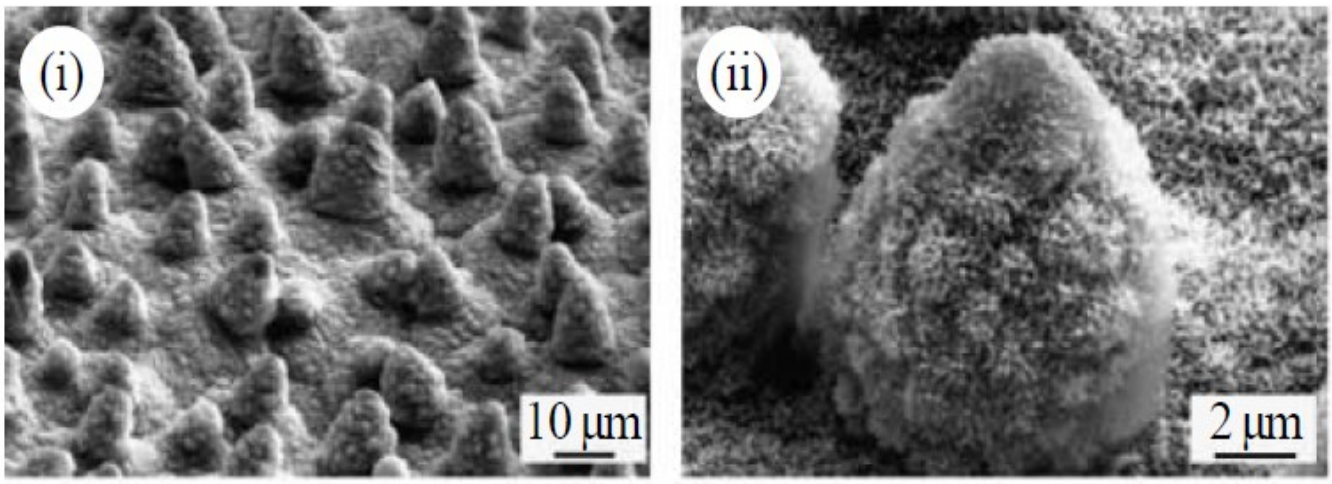

Figure 2-3. SEM images of Lotus leaf in two different magnifications [15]

Superhydrophobic surfaces, where a combination of low surface energy and surface texturing is used to increase the water-repellency, have attracted worldwide attention for their potential applications [16]. Some of these applications include dropwise condensation [17], anti-icing [18], self-cleaning [19] and corrosion resistance [20].

As the primary focus of this study is the potential application of superhydrophobic coatings in condensation and corrosion resistant graphene coatings, most of the literature was reviewed on condensation and corrosion resistant coatings.

2.2.4. Effect of surface roughness on wetting

Beside surface chemistry, the surface roughness is another factor that has a critical influence on the wetting behaviour of solid surfaces. The water droplet contact angle on a rough surface due to the formation of air pockets between the liquid and solid is different from the contact angle on a smooth surface of the same material. Once the water droplet forms on these air pockets the contact angle increases [13].

Understanding the droplets behaviour on a surface can be determined by measuring the contact angle. Nevertheless, Young's equation assumes a quite ideal solid surface, and it does not consider the other significant properties of real surfaces. Wenzel and Cassie-Baxter [21] proposed two models that continued Young's work covering the wetting study to rough and porous surfaces. The first model developed by Wenzel assumes a homogenous, smooth, water-solid interface. In the Wenzel state, the droplet entirely wets all of the rough areas, and no air bubbles are present between the solid and liquid. The Wenzel equation magnifies the contact angle by a factor r, as shown in Eq.2.2.

$$\cos\theta_W = r\cos\theta_0 \qquad \text{Eq. (2.2)}$$

The other model suggested by Cassie and Baxter assumes a composite water-solid-air interface. Contact angle, in this case, is defined by Eq.2.3, where *f* is the surface roughness fraction [22]. A schematic of the two models is demonstrated in Figure 2-4

$$\cos\theta_c = f(\cos\theta_0 + 1) - 1 \qquad \text{Eq. (2.3)}$$

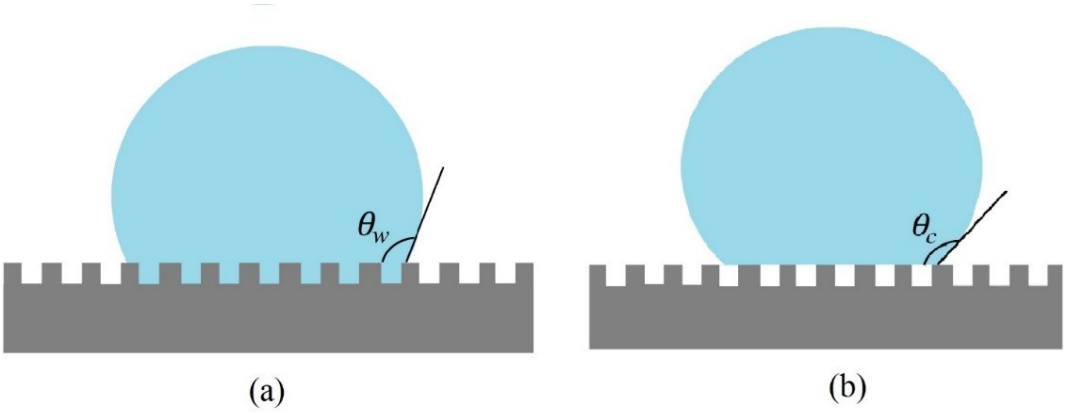

Figure 2-4. Schematic of (a) Wenzel and (b) Cassie-Baxter state

In both cases, the chemical characteristics of the surface are intensified by roughness. When the primary wetting state is Wenzel, an intrinsically hydrophilic surface becomes more hydrophilic, and an intrinsically hydrophobic state becomes more hydrophobic. Generally, the adhesion between water and solid surface in this state is high. Subsequently, water mobility in the Wenzel state is usually poor therefore the Wenzel state is less desirable [23]. Nevertheless, in the Cassie-Baxter wetting state, due to the presence of air pockets between the solid and liquid phases, the wettability of a surface decreases.

As a result, an intrinsically hydrophilic surface may also show hydrophobic behaviour when roughened in an appropriate method to produce a Cassie-Baxter wetting state. Therefore, many studies have concentrated on the Cassie state to reduce the adhesion in superhydrophobic surfaces [24]. The wettability of a surface is defined by both its surface micro-texture as well as its chemical composition. Figure 2-5, shows the wettability behaviour difference for smooth, micro-textured, nanotextured and hierarchically textured surfaces. The contact angle is the highest in the hierarchical texture while the smooth surface shows the smallest contact angle. A hierarchical surface structure similar to the natural superhydrophobic surfaces of a lotus leaf leads to a Cassie-Baxter interface [25].

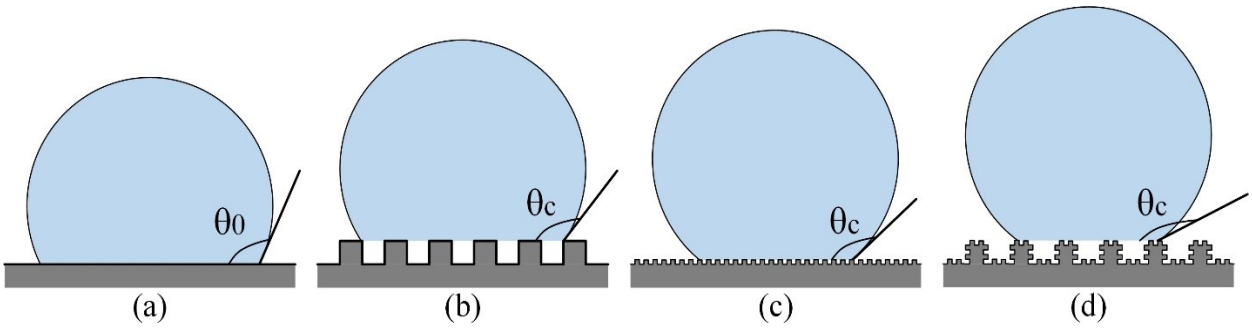

Figure 2-5. Schematic for wetting of (a) smooth, (b) micro-textured, (c) nanotextured and (d) hierarchically textured solid surfaces [13]

2.3. Graphene-based composites as coatings

Graphene, a new generation material, is a carbon allotrope which was first discovered by mechanical exfoliation in 2004 [26]. It is a two-dimensional honeycomb single-layer crystal lattice

made of the closed packed sp^2 bonded carbon atoms. The unique structure of graphene results in remarkable electrical properties such as high electron mobility. Also, graphene has excellent optical properties, extraordinary mechanical properties (Young's Modulus: 1TPa and tensile strength: 130 GPa) and excellent thermal conductivity of 5000 $Wm^{-1}K^{-1}$ at room temperature. Nanocomposites, energy storage devices, barrier applications, and so forth are some potential applications of graphene suggested by researchers [27].

2.3.1. Copper-graphene composites

Copper matrix composites present a broad range of applications in electronics, thermal devices and structural materials due to their excellent thermal and electrical conductivity as well as their outstanding mechanical properties. One of the main setbacks of ceramic fibres and particles is that they decrease the thermal and electrical conductivity for copper matrix composites. Graphene with its excellent electrical, thermal and intrinsic ultrahigh mechanical properties is considered to be one of the most promising reinforcements of copper matrix composites [28][29]. For instance, high-quality graphene coated copper powders by ball milling has been reported to improve the electrical conductivity of a copper/graphene composite [30].

Li et al. [31] reported an electrical conductivity improvement in copper/graphene composite based on high-quality graphene. With the ball-milling process (Figure 2-6) and subsequent spark plasma sintering, graphene-coated copper powders were produced. The results showed the electrical conductivity of the Cu-G composites is significantly enhanced while the highest electrical conductivity of the Cu-G composite was achieved at the optimal 1 wt. % of graphene, at which an 8% increase in electrical conductivity was obtained when compared with pure copper. They associated the electrical conductivity improvement to the high electron mobility of graphene and the formation of a graphene conductive network in the Cu-G composites. Furthermore, results revealed that the hardness of the Cu-G composites was much higher than that of pure copper.

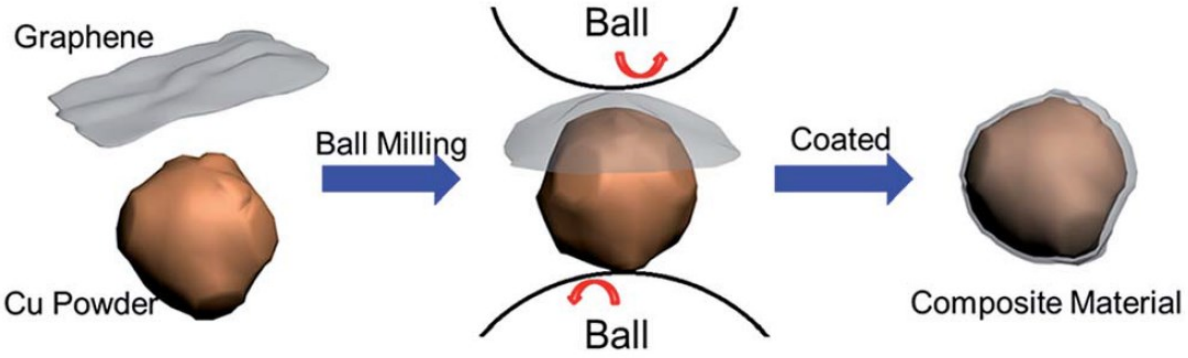

Figure 2-6. Schematic illustration of the fabrication process for the copper/G composite by ball milling [31]

In this work, the main focus that will be presented in this section is on the application of graphene coatings, graphene-based superhydrophobic surfaces and corrosion resistance graphene coatings.

2.3.2. Application of graphene in coatings

Some potential applications of graphene are already mentioned in the previous sections. Additionally, the outstanding properties of graphene can improve the performance of coatings considerably. Moreover, graphene can be used with other particles to form graphene-based composite coatings. It is used as a filler in polymer matrix nanocomposites to improve the mechanical properties of the coatings [32]. Graphene is believed to be a promising coating to reduce wear and friction on substrate surfaces. It is reported by Diana Berman et al. [33] that adding a small amount of graphene leads to significant reduction in wear and friction coefficients on sliding steel surfaces.

2.3.3. Graphene-based superhydrophobic coatings

As previously mentioned, both chemical composition and surface texture influence the wetting behaviour of a solid surface. Researchers are inspired to produce superhydrophobic textured surfaces like a lotus leaf. Superhydrophobic surfaces can be logically produced by combining hierarchical roughness and low-surface-energy materials [1]. These surface treatments are typically achieved by functionalizing the surface with a hydrophobic coating. Most of these

coatings face challenges when dealing with practical applications like condensation. Since intrinsically hydrophobic materials are generally polymers, thin layers with slightly increased thermal resistance are not durable and have low chemical stability.

On the other hand, thicker polymer coatings, with more durability, characteristically, increase the thermal resistance enormously which is not desirable for dropwise condensation [34]. Moreover, many polymeric materials are subjected to degradation and may cause some environmental issues. Such challenges have generated an increase in the usage of graphene in superhydrophobic surfaces. In some recent publications [35][36] graphene has been reported to be inherently hydrophobic. On the other hand, some other publications have disputed this [37][38] by arguing that airborne contamination of hydrocarbons is the main reason for apparent hydrophobicity of graphene.

Although the subject of intrinsic hydrophobicity of graphene is debatable, it could potentially improve the mechanical properties of superhydrophobic coatings such as wear and corrosion resistance. Graphene, when compared to polymeric and hydrocarbon options, is much more durable. The hydrophobicity of graphene is further studied in this work. So far, there is a lack of a surface engineering technique to produce micro-textured surfaces with a hierarchical roughness which is optimal regarding practicality, repeatability, ease of applicability, durability and scalability to large surfaces. The purpose of this work is to use thermal spray processes to fabricate such coatings. Therefore, in the following section, a literature review of graphene-based superhydrophobic coatings is presented. As mentioned previously, graphene is recognized as a high water repellent material while graphene oxide (GO) is hydrophilic [39][40]. The intrinsic hydrophobic property of graphene makes it appropriate for water repellant applications.

Recently at Rice University, a perfluorododecylated graphene nanoribbon (FDO-GNR) film has been designed that has the low polarizability of perfluorinated carbons and the conductive nature of graphene nanoribbons at the same time. The FDO-GNR films are superhydrophobic with an anti-icing property that avoids freezing of cold water. Voltage is applied to the films to de-ice the surface which resulted in reaching a water contact angle of 161°. The anti-icing and de-icing properties of the FDO-GNR films are promising for use in cold environments [41].

In another study, Nine et al. [42] prepared graphene-based multifunctional superhydrophobic composite coatings with robust mechanical strength, self-cleaning, and barrier properties. The produced coating showed stability as well as mechanical reliability even after

sandpaper abrasion and crosscut scratching. Moreover, excellent corrosion resistance properties were observed by studying a potentiodynamic polarization. In order to further evaluate the coating barrier properties, acid was used. The results revealed significant improvement in the barrier performance for a small amount of reduced graphene oxide additive. As a final point, the achieved coating presented a self-cleaning feature.

Nguyen et al. [43] reported a new strategy to fabricate graphene-based sponges with both superhydrophobic and superoleophilic properties by a straightforward and inexpensive dip coating method. Hydrophobic graphene nanosheets were controllably attached on the sponge and exhibited exclusive properties such as outstanding absorption capacities, high selectivity, excellent recyclability, lightweight, robustness, and inertness to corrosive environments.

Zhang et al. [44] produced the graphene/polyurethane (G-PU) sponge by simply dip-coating PU sponges in graphene aqueous suspension containing cellulose nanowhiskers as a dispersant. The superhydrophobic GN-PU sponge presented densely packed graphene sheets, contributing superhydrophobicity to the sponge with a water contact angle of 152°. Once coated with thin graphene layers, the mechanical durability, thermal and chemical stability were all improved significantly.

2.3.4. Corrosion resistant graphene-based coatings

Graphene is also demonstrated to be an active corrosion barrier material due to its inert structure under the conditions where chemical reactions of other substrates will occur [18]. Thus, it is also promising to enhance the corrosion resistance property of a coating system. An anti-corrosion mechanism of CVD graphene coating on a copper substrate was suggested by Singh Raman et al. [45]. The result showed improvement in the resistance of the Cu to electrochemical degradation. The schematic of the corrosion resistance mechanism of their work is shown in Figure 2-7.

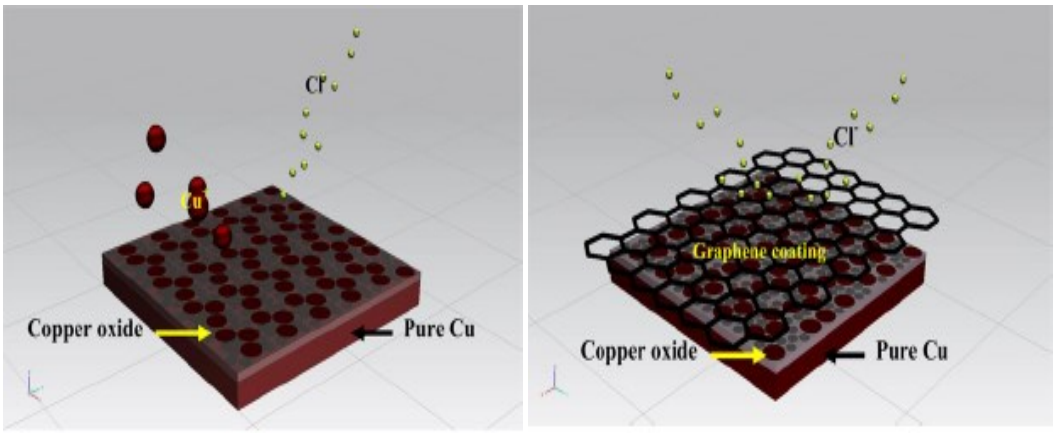

Figure 2-7. Schematic of anti-corrosion mechanism of CVD graphene coating on copper [45]

In another work by Sai Pavan et al. [46] graphene nanosheets were produced by the Hummer's method in 1-propanol to develop a coating solution. The coatings were formed on steel coupons with the dip coating method. Corrosion studies were performed at different environments like water (pH 6.0), HCl (0.1 N), NaCl (3.5 wt. %) and NaOH (1 M). Tafel analysis displayed a decrease in the corrosion rate up to 99 % after three layers of deposition with the graphene in all environments. As illustrated in Figure 2-8, increasing the number of deposited graphene layers decreased the corrosion rate considerably.

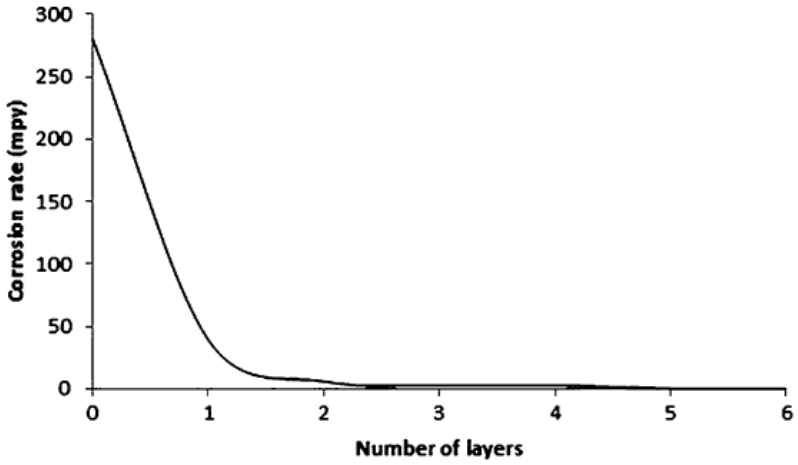

Figure 2-8. Corrosion rate (mm / year) decrease with increasing number of graphene layers deposited [46]

2.4. Coating methods

In this section, a brief introduction to graphene-based coating methods is presented followed by a more detailed discussion of atmospheric plasma spraying (APS) and high-velocity oxy-fuel (HVOF) which are the two thermal spray techniques used in this work. Different coating methods have their advantages and limitations. Some of the techniques currently being used are the following:

Dip coating [47] is an easy method to coat thin film on a substrate. Nevertheless, it is inapplicable for industrial procedures owing to the inconsistent coating quality. For graphene-based composite coatings, the thickness distribution can be challenging. The coating film fabricated through the sol-gel approach [48] tends to form cracks easily. There is also a thickness limitation of each layer (about 1 micron). A pure and dense coating can be fabricated through a CVD process. This method has some restrictions such as safety and hazard issues caused by the precursor gases, difficulties of depositing compound materials and expensive equipment [49][50].

Electrophoretic deposition [51] is an appropriate method to produce high-quality graphene coatings. A significant amount of work is required to determine the best conditions for different coating applications. This technique is more appropriate to produce pristine graphene-based coatings. Spray coating [52] is another method extensively used in industrial applications. Thermal spray process can be considered as a potential method to produce graphene-based superhydrophobic surfaces. However, establishing the window of operation to produce such coatings with different parameters needs to be evaluated.

2.4.1. Thermal spray process

As previously mentioned, in order to produce a superhydrophobic surface a hierarchical texture and a low surface energy material are required. Atmospheric plasma and high-velocity oxy-fuel (HVOF) spraying are considered as outstanding methods of producing microstructured coatings using different materials. Furthermore, thermal spray processes are shown to be cost-effective methods of surface engineering. Consequently, the thermal spray process can be applied to fabricate superhydrophobic surfaces for industrial applications.

In thermal spray processing, a heat source, which can be chemical combustion or electrical, is applied to melt feedstock materials that are pushed at high velocities toward a substrate by a stream of gas or an atomization liquid jet. A coating will be then formed by the impact of the semi-molten or molten particles on the substrate. Subsequently, flattening, cooling and solidification of the droplets will take place [53]. The surface morphology, microstructure and porosity of the coatings can be optimized by applying different spraying parameters in thermal spray techniques [54]. Figure 2-9 compares the temperature, and velocity ranges of the particles for different thermal spraying techniques including cold spray, high-velocity oxy-fuel (HVOF), plasma spray and flame spray.

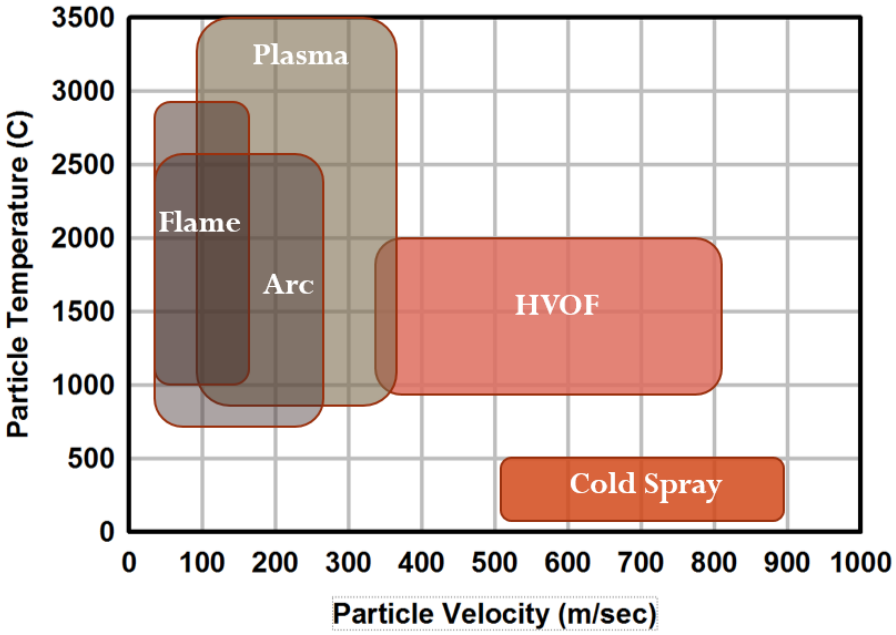

Figure 2-9. Particle velocity and gas temperature for thermal spray processes [55]

2.4.1.1. Atmospheric Plasma Spray

Atmospheric plasma spray (APS) is one of the most versatile of all the thermal spray processes because of its wide application on numerous base materials and with a variety of powders. In this process, a strong electric arc is generated between a tungsten cathode and a copper anode by ionization of a jet of primary gas (argon or nitrogen) mixed with a secondary gas (hydrogen or helium). Once the plasma plume is formed, the powder particles with an average particle size ranging typically from 10 to 100 µm, are introduced into the high-velocity and high-

temperature plasma jet via a carrier gas (e.g. argon) and melt. Later, by acceleration, impact, flattening and deposition of the molten particles on the substrate's surface, the coatings are formed. The gases used to generate the plasma and the applied current are the most useful parameters controlling the input power. In this process, the flame temperature can be as high as 15000°C which makes a wide variety of coating materials suitable as the starting powder. One of the drawbacks of this process is the oxidation of some of the molten particles in its atmospheric environment [53][56]. A schematic view of this process is illustrated in Figure 2-10.

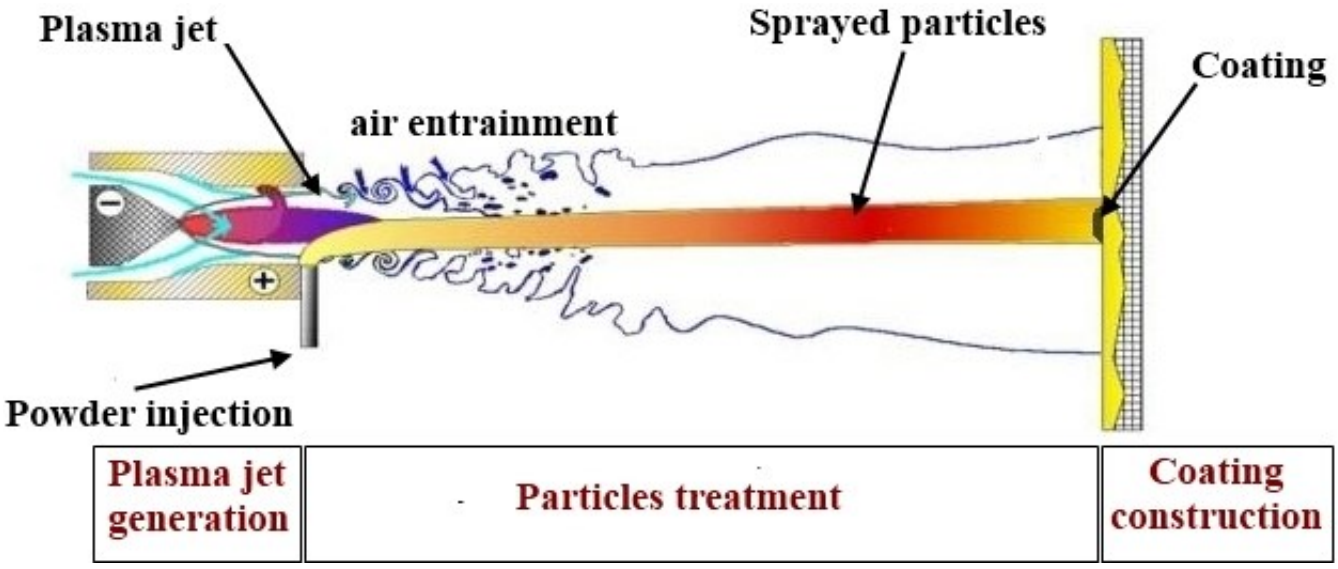

Figure 2-10. A schematic of atmospheric plasma spray technique [57]

2.4.1.2. High-velocity oxy-fuel (HVOF)

At the beginning of the 1980s, another thermal spray process, the high-velocity oxy-fuel (HVOF) was introduced. This process with its higher particle velocities and relatively lower temperature led to the formation of coatings with a low-oxide content compared to plasma spray [58].

In the HVOF process, oxygen and one of a select group of ignitable materials (hydrogen, propylene, propane, acetylene or kerosene) are mixed and injected into a combustion chamber and

subsequently ignited and combusted. First, the exhausted gas accelerates in a converging-diverging nozzle and then it emerges into the atmosphere at supersonic velocities. Shock diamonds are formed at the exit of the nozzle which occurs when the high-velocity flow (500 to 1200 m/s) at the exit of the nozzle, expands. The pressure in the combustion chamber (typically 0.3 to 1 MPa) mainly affects the gas velocity. The typical powder particle size in this process is in the range of 5-45 μm which can be injected radially or axially into the gas by nitrogen or argon as the carrier gas. The coating is formed after acceleration, melting and deposition of the fully melted or partially melted particles on the substrate's surface. The high velocity of this process leads to coatings with high density and excellent adhesion [53] . A schematic of a typical HVOF system is presented in Figure 2-11.

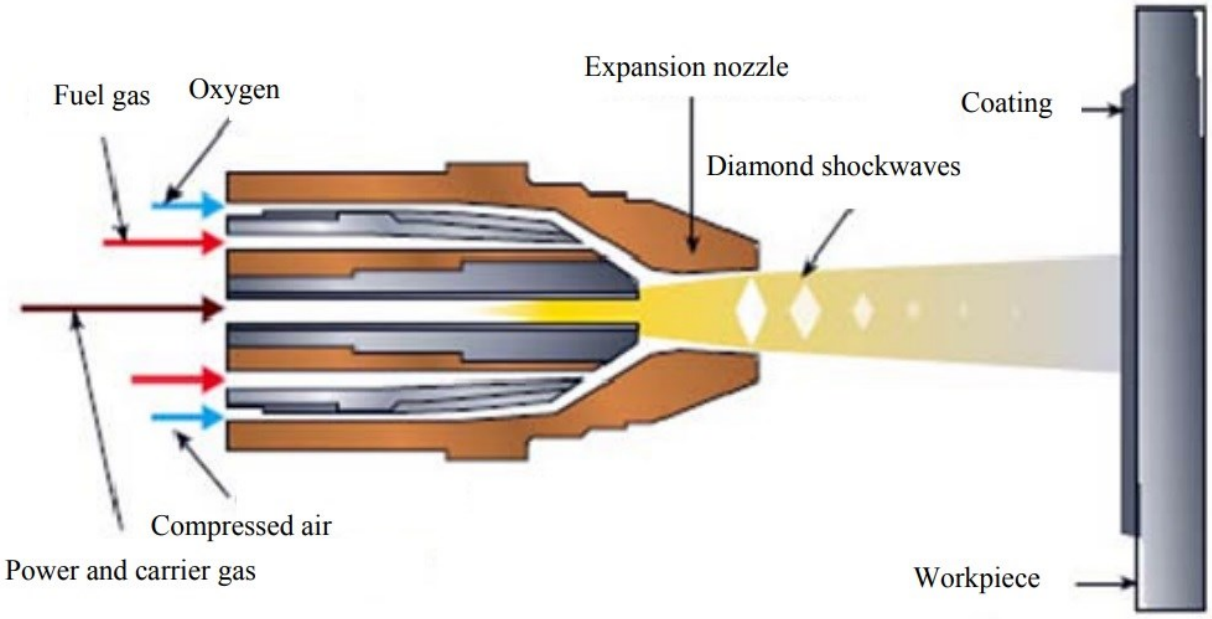

Figure 2-11. A schematic of the high-velocity oxy-fuel technique [59]

2.4.2. Thermal spray processes for graphene-based composite coatings

Several studies have been conducted on using different thermal spraying techniques for development of graphene-based coatings. Liu et al. [60] deposited graphene nanosheet reinforced hydroxyapatite (HA) composites with enhanced biocompatibility via cold spraying. The coatings were uniform in thickness and results revealed improved adhesive strength and fracture toughness due to uniformly embedded graphene nanosheets in the HA matrix.

In another report by Ward et al. [61], multilayer graphene oxide (GO) was used as a reinforcement. Improvement in hardness and tensile adhesion strength, as well as a reduction of residual strain and coefficient of friction, was reported. In this article, it was demonstrated that GO could successfully be preserved as an additive in thermal spray coatings for low-cost industrial applications. Li et al. [62] produced zirconia-graphene nanosheet composite coatings by plasma spraying. Results showed improvement in wear resistance and lowered friction compared to pure zirconia. GNP reinforcement was shown to be even more effective than graphite reinforcement in reducing wear rates. In 2017, Murray et al. [63] proposed alumina-graphene nanocomposite coatings fabricated by suspension high-velocity oxy-fuel thermal spraying for ultra-low-wear. They reported an improvement of two orders of magnitude in the specific wear rate by adding a small weight percentage (1 Wt%) of GNP to a suspension high-velocity oxy-fuel alumina coating.

Youtao Xie et al. [64] studied calcium silicate coatings with different graphene contents fabricated by vacuum plasma spraying technology for load-bearing implant surface modification. The surfaces of the coatings displayed a hierarchical nano /microstructure, which is helpful to the behaviours of the cell and early bone fixation of the implants. The wear resistance of the composite coating was improved by the reinforcement of GPs. The same group also reported [65] the excellent survival of the GPs in the composite coating confirmed by Raman analysis. Moreover, they linked the reinforcement mechanism to the enhanced micro-hardness and interfacial bonding of the particles in the coating.

In most of these studies, the main focus was on improving the mechanical properties of the coating. Nonetheless, the effect of the spray parameters, different coating methods and surface modifications was not addressed in detail to promote the desired microstructure. Modification and engineering of the process could resolve the issue associated with the graphene combustion by optimization of the coating parameters which has not been comprehensively addressed in the literature.

Chapter 3. Experimental Procedure

Despite outstanding properties, single layer graphene has high production costs for large-scale applications like metal surface protection due to the available deposition methods. To lower associated production costs, potentially attractive alternatives like graphene nanoplatelets have been suggested which exhibit graphene-like properties with inexpensive production techniques [66].

This work was performed with copper and graphene nanoplatelets particles. This mixture was chosen to overcome the two most critical challenges of depositing pristine graphene through thermal spray processes. Firstly, the graphene structure when exposed to elevated temperatures in an atmospheric environment can quickly react with oxygen and lose its characteristics. Secondly, graphene nanoplatelets are very small and have low density therefore have a small mass. Even during perfect injection conditions, while travelling through the supersonic jet in HVOF or the plasma jet in APS, they are highly unlikely to get deposited on the substrate as they follow the gas streamlines near the substrate.

Consequently, it is essential to mix and create a composite powder of copper and graphene before introducing the powder into the supersonic jet. The copper plays two roles in this scenario: first, it protects the graphene structure from destructive interactions with air and second, it acts as a higher density carrier that transfers the graphene nanoplatelets to the target. Considering that the material of interest as a substrate is copper, using copper/graphene nanoplatelets composite feedstock can present additional benefits, namely improved adhesion and mechanical and physical properties of the coatings. The potential application is for dropwise condensation heat transfer. However, this work is focused on the microstructure of the coating produced by thermal spray processes and not heat transfer performance.

The scope of this investigation is to determine possible operating conditions to deposit the powder mixture on copper substrates. The challenges of this work are the complexity of the process and sensitivity of the GNP to high heat and deposition condition. This chapter describes in detail

the experimental procedure performed in this work. Coatings were sprayed on substrates with two processes: APS and HVOF. All the spray parameters applied and the experiments performed are described in the following sections.

3.1. Substrate preparation

The substrate material of the samples used in this work was copper (McMaster-Carr, USA). All the coatings were deposited on a 2.54 × 2.45 × 0.3 cm flat, square, copper substrates to evaluate the microstructure of the high-velocity oxy-fuel, and atmospheric plasma sprayed coatings. Prior to the coating process, all the substrates were grit-blasted with aluminum oxide (Al_2O_3) grit size of 180 and air pressure of 354 kPa generating a surface roughness of Ra ≈ 1.8 μm. The roughness was measured with a profilometer (Mitutoyo, Japan) in the center of the samples, in the same orientation of the scanning of the plasma torch. Afterwards, the samples were ultrasonically cleaned in acetone and dried with compressed air to eliminate contamination. Figure 3-1 shows the substrate before and after grit blasting and the substrate holder used for the coating process. Once the samples were placed on the sample holder, the latter was fixed to the table inside the spray booth, ready to be sprayed.

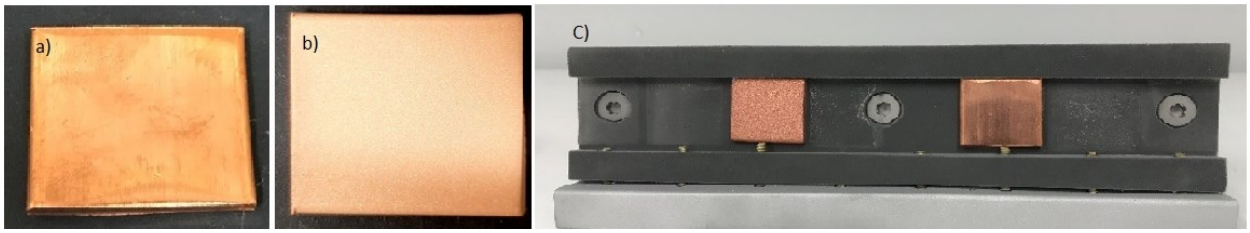

Figure 3-1. (a) Smooth copper substrate, (b) grit-blasted substrate, and (c) the substrate holder

3.2. Feedstock preparation

A Cu-GNP mixture was chosen as the feedstock for this work to improve hydrophobicity as well as mechanical properties as a composite [67]. As previously mentioned, it is particularly challenging to inject graphene nanoplatelet powder into a powder feeder and subsequently into the APS and HVOF plumes. Due to its small mass, GNP powder does not have the required momentum to deposit on the substrate. Moreover, graphene at high temperatures in an atmospheric

environment can eagerly react with oxygen and lose its characteristics. Consequently, it is necessary to mix and create a composite powder of copper and graphene before introducing the powder into the supersonic jet.

Commercial copper powders (Metco™ 55, and Diamalloy 1007) were used as the feedstock for the APS and HVOF coating procedures, respectively. SEM micrographs of the as-received copper are presented in Figure 3-1. In the SEM micrograph, copper particles are shown to have a spherical morphology. GrapheneBlack™ 3X (Nanoxplore Inc., Canada) which is a versatile and low-cost graphene powder with an average flake size of 38 µm with thicknesses mainly ranging from 6-10 layers was used as a reinforcement. A TEM image of as-received GNP is presented in Figure 3-3 showing the multilayer structure of graphene nanoplatelets.

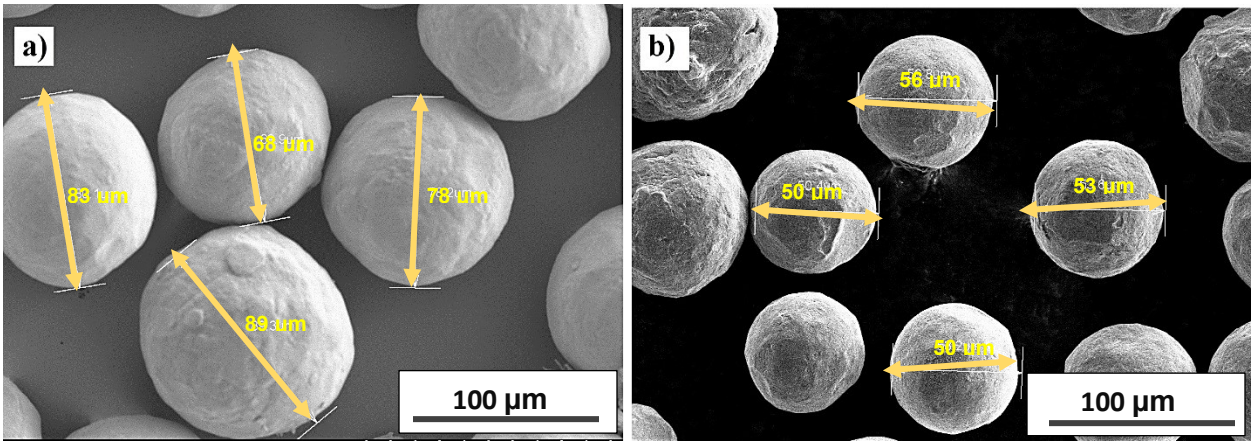

Figure 3-2. As received copper powders, spherical morphology a) Metco™ 55 b) Diamalloy

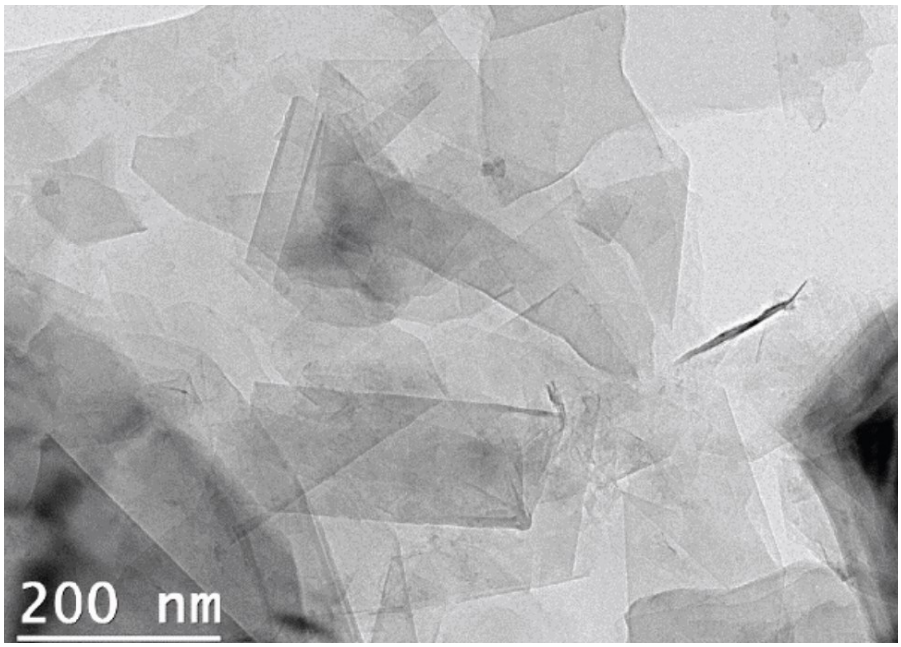

Figure 3-3. TEM image of few-layer thick graphene flakes mainly from 6 - 10 layers

(Supplied by Nanoxplore Inc.)

To prepare the feedstock, 2 wt. % graphene nanoplatelets (GNP) were dispersed in ethanol for 1 hour to achieve a uniform dispersion by ultrasonication at a frequency of 10 kHz and pure copper powders were then added. Then, the mixture of GNP and pure copper powder was ball-milled at a rotational speed of 250 rpm for 3 hours. Stainless steel balls with a ball-to-powder ratio of 5:1 were used in a planetary ball mill. The mixed powders were then dried in an oven at 80°C to remove ethanol. A schematic of the Cu-GNP composite preparation is presented in Figure 3-4.

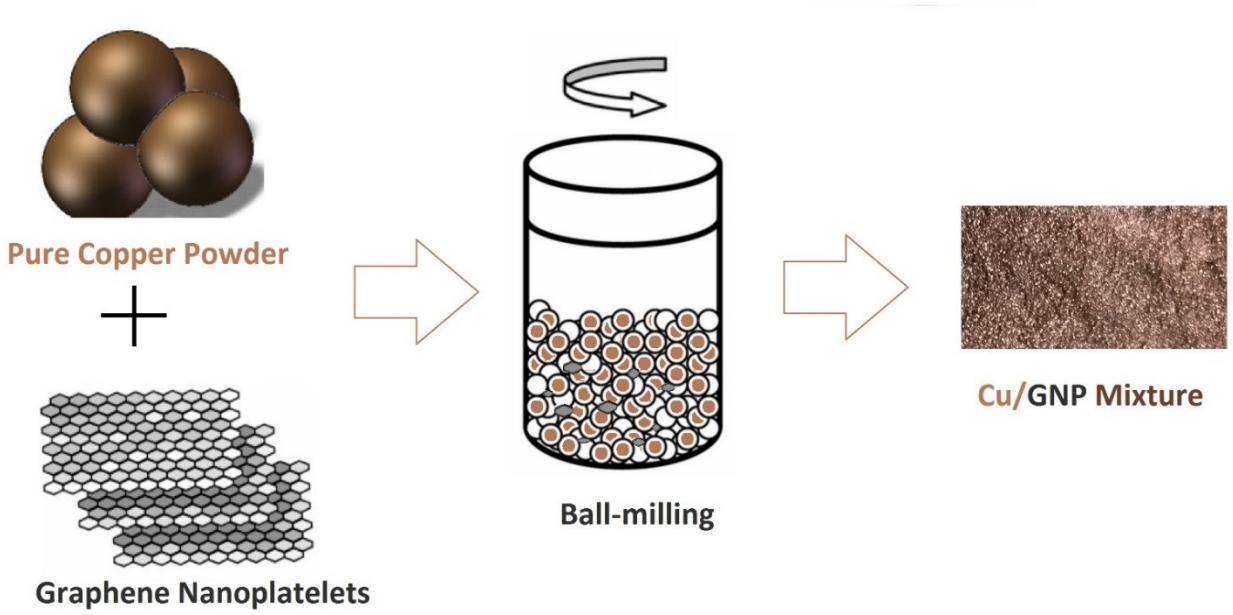

Figure 3-4. Schematic of the Cu-GNP composite preparation

The particle size distributions of all the powders were measured by a laser diffraction particle size analyzer (Malvern Instruments Ltd., England). Particle size distribution of the Cu-GNP mixture for APS (illustrated in Figure 3-5) and size distribution characteristics of the two feedstock powders used in the APS process (given in Table 3-1) revealed that the milled powders showed a noticeable size reduction. The total large surface area of GNP can reduce the contact area between the Cu particles during the ball milling, which would then prevent the cold-welding of Cu particles. This indicates that the graphene nanoplatelets can play a helpful role as grinding agent due to its small size and wrinkled structure, which can successfully prevent the agglomeration of mixture powders. Such prevention of the particle agglomeration facilitates the homogeneous distribution of the GNP within the Cu matrix.

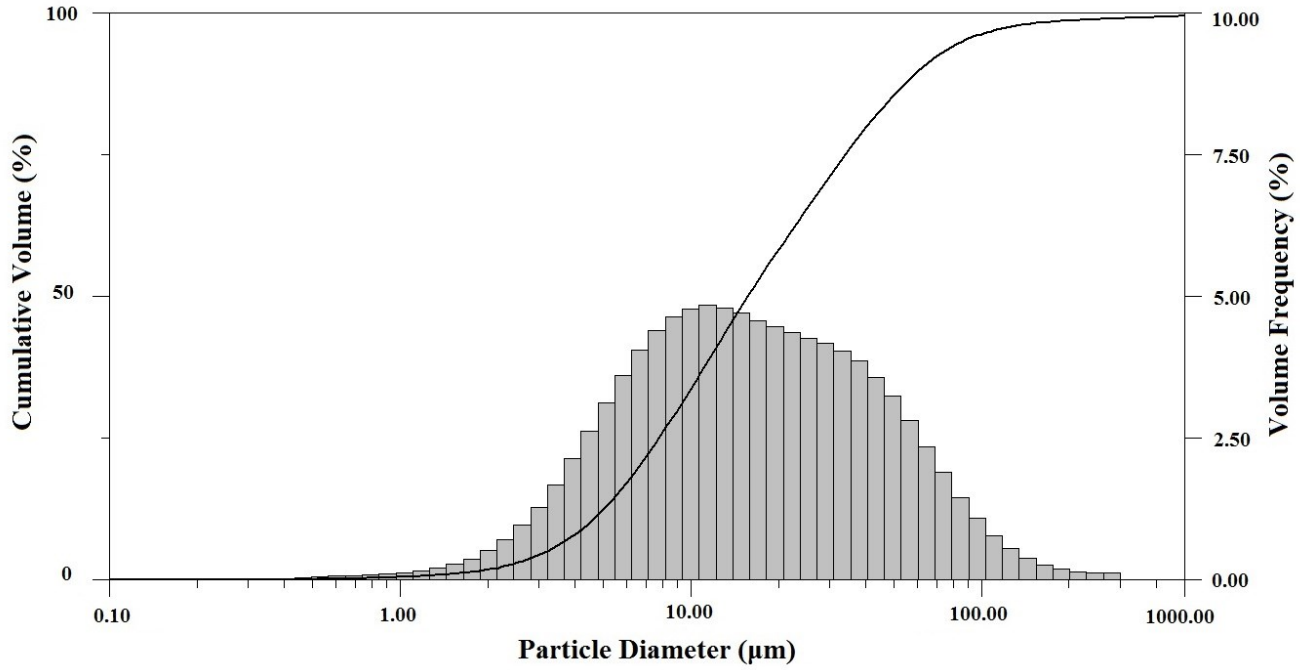

Figure 3-5. Particle size distribution of Cu-GNP for the APS process.

Table 3-1. Size distribution characteristics of the two feedstock used in the APS process.

The standard deviation value is "±1"

Powder	D_{10} (µm)	D_{50} (µm)	D_{90} (µm)
Copper	49	67	91
Copper/Graphene Nanoplatelets	4.5	16	61

The morphology of the fabricated Cu-GNP composite powder (2.0 Wt. % GNP) can be seen in the SEM image presented in Figure 3-6. As shown, the fabricated composite powders exhibited a layered flake-like structure. The spherical morphology of the first Cu matrix powder changed into the flake morphology due to the high-energy impact resulting from the ball-powder-ball collisions. Feedstock particles are shown to have a homogeneous distribution of graphene embedded in the copper matrix. This might cause the roughness of the coating to increase, especially for partially molten particles.

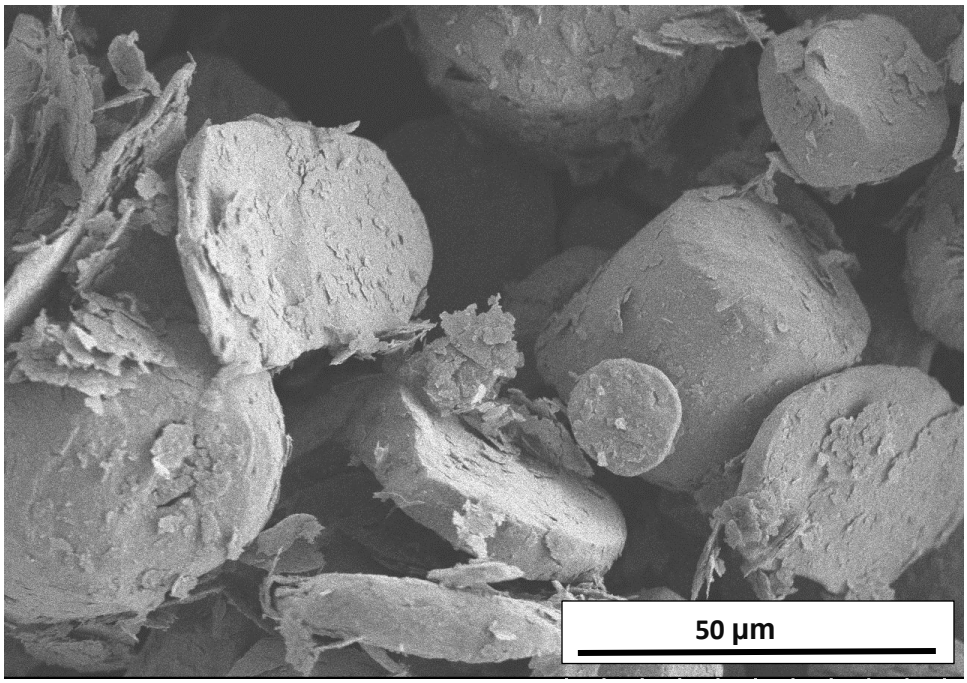

Figure 3-6. The flake-like morphology of the Cu-GNP feedstock.

The particle size distribution graph of Cu-GNP feedstock for HVOF process is shown in Figure 3-7 and size distribution characteristics of the two feedstock used in this process are presented in Table 3-2. Results showed again a significant average size reduction of the Cu-GNP powder compared to the pure copper.

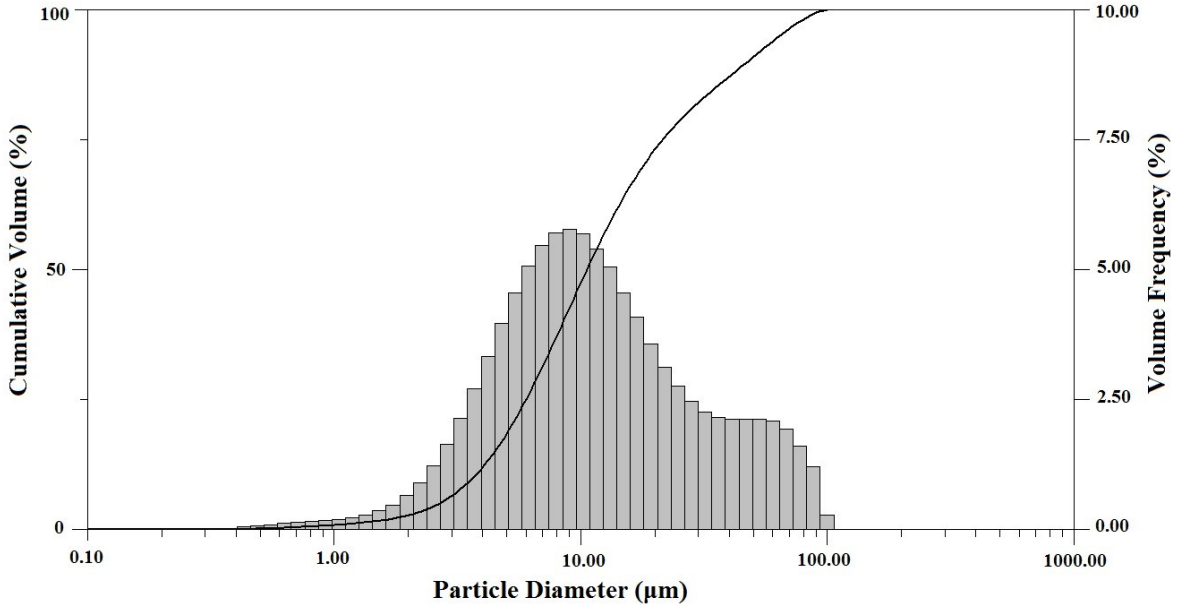

Figure 3-7. Particle size distribution of the Cu-GNP mixture for HVOF process

Table 3-2. Size distribution characteristics of the two feedstock used in the HVOF process.

The standard deviation value is "±1"

Powder	D_{10} (µm)	D_{50} (µm)	D_{90} (µm)
Copper	49	61	75
Copper/Graphene Nanoplatelets	3.5	10	47

Two different methods of milling including dry milling and wet milling with ethanol were used. Dry milling did not show promising results to retain the graphene. Even after 10 minutes of dry milling as shown in Raman spectra in Figure 3-8, the intensity of the D (1350 cm^{-1}) peak increased hence showing an increase in the amount of disorder in graphene. The D peak intensity is an indicator of the number of defects in the carbon material. Increased D peak intensity means increased defect density and edges [68].

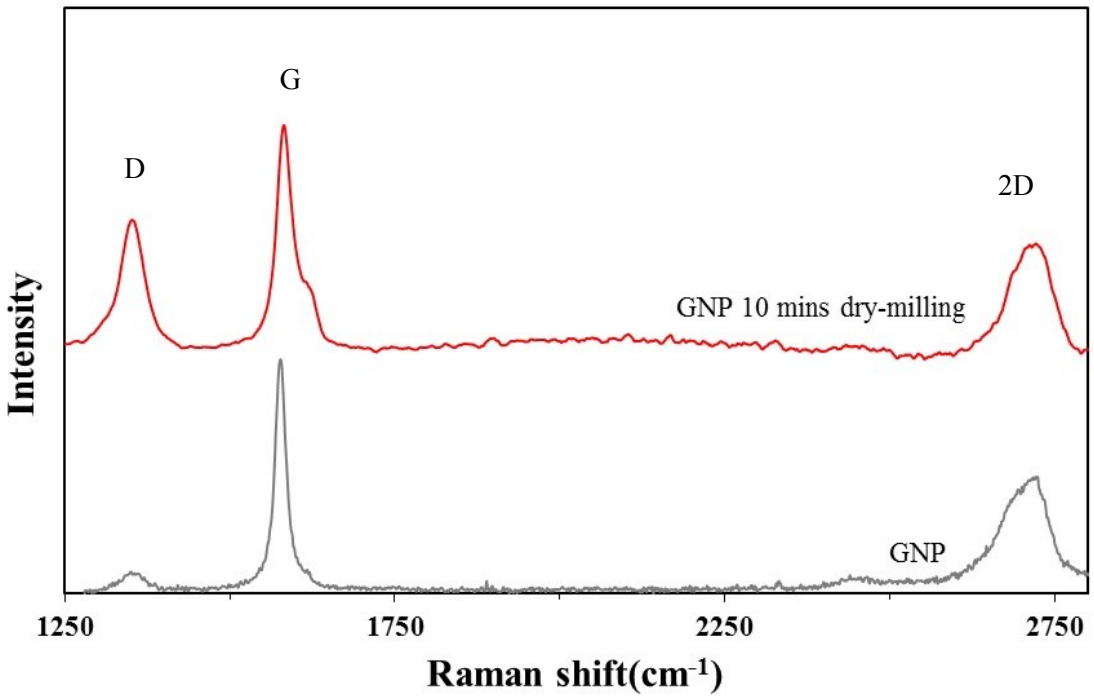

Figure 3-8. Raman spectra of the Cu-GNP powders after10 min of dry milling

The wet-milling process which was performed with a control agent (ethanol) showed no changes to the peak intensity after 10 minutes. However, after 3hrs of wet milling, the D peak intensity increased slightly but, still less than the change that occurred after 10 minutes of dry milling (Figure 3-9).

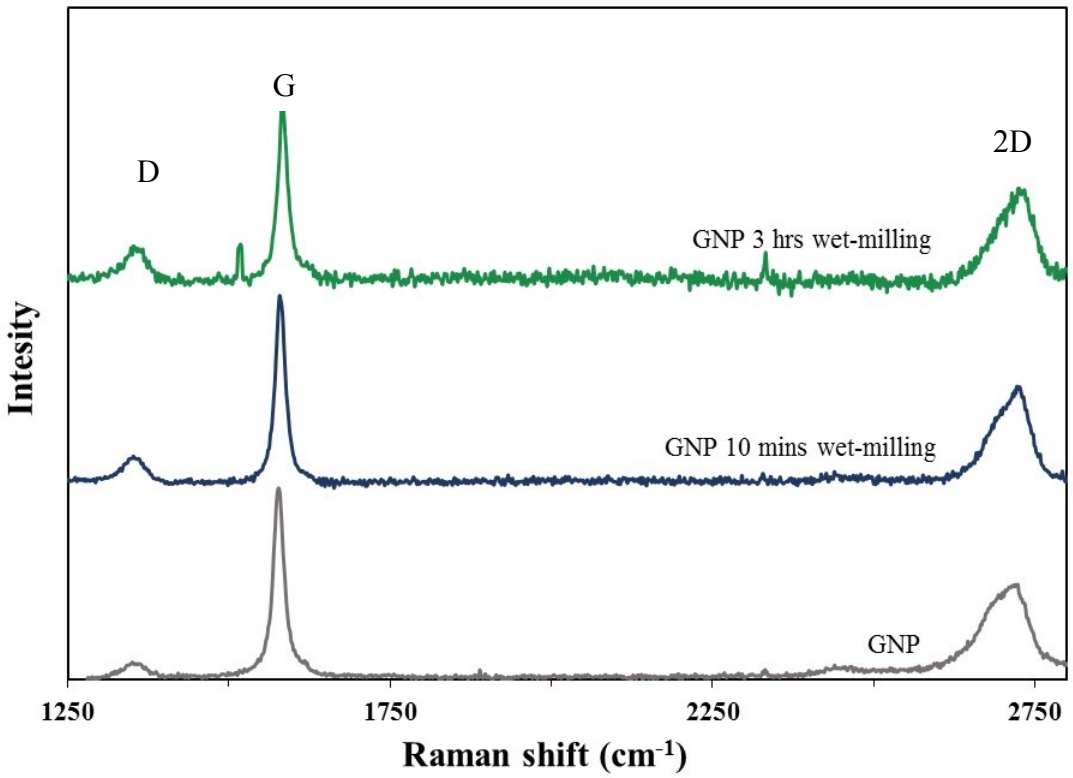

Figure 3-9. Raman spectra of the Cu-GNP powders milling in ethanol

3.3. Design of experiments

To produce Cu-GNP coatings two spray processes APS and HVOF were used. After that all the coated samples were treated with stearic acid in a similar way. In total, 12 types of samples were studied, combining the spray processes, surface treatments and plasma power. The samples were labelled as presented in Table 3-3.

Table 3-3. Design of experiments of samples sprayed

Sample	Type of Deposition	Coating Material
B-Cu	Bare Cu (no treatment)	-
Cu-S	Dip Coating	Stearic Acid
Cu-LP-APS	Low Power APS	Copper
Cu-MP-APS	Medium Power APS	Copper
Cu-HP-APS	High Power APS	Copper
Cu-GNP-LP-APS	Low Power APS	Copper/Graphene Nanoplatelets
Cu-GNP-MP-APS	Medium Power APS	Copper/Graphene Nanoplatelets
Cu-GNP-HP-APS	High Power APS	Copper/Graphene Nanoplatelets
Cu-LR-HVOF	Low Ratio Oxy-fuel HVOF	Copper
Cu-HR-HVOF	High Ratio Oxy-fuel HVOF	Copper
Cu-GNP-LR-HVOF	Low Ratio Oxy-fuel HVOF	Copper/Graphene Nanoplatelets
Cu-GNP-HR-HVOF	High Ratio Oxy-fuel HVOF	Copper/Graphene Nanoplatelets

Many parameters affect the structure and morphology of APS coatings. In order to obtain repeatable APS coatings, it was decided to focus on the plasma secondary gas (hydrogen) flow rate and consequently, the temperature of the particles during the process and upon impact with

the substrate. In order to minimize the particle temperature, some modified parameters from previous studies [69] were used and kept constant. The APS process parameters used to spray the samples in this work are described in Table 3-4.

Table 3-4. APS coating parameters

Parameters	Low Power	Medium Power	High Power
Standoff distance (cm)	12	12	12
Feed rate (g/min)	22	22	22
Hydrogen flow rates (NLPM)	0	3	5
Plasma Power (kW)	18	25	32
Argon flow rate (NLPM)	75	75	75
Current (A)	500	500	500
Injecting angle	90° +20°	90° +20°	90° +20°

Three different hydrogen flow rates with their respective plasma powers of 18 kW (LP), 25 kW (MP) and 32 kW (HP) were selected. The standoff distance was kept constant for all the experiments at an operational distance of 12 cm in front of the substrates to minimize the substrate temperature. It should be noted that during all the experiments, the feedstock injection was radial, external to the plasma gun with the injector oriented 20° towards the substrate to reduce the particle temperature and allow GNP retention as shown in Figure 3-10. The injection feed rate was kept constant for all experiments.

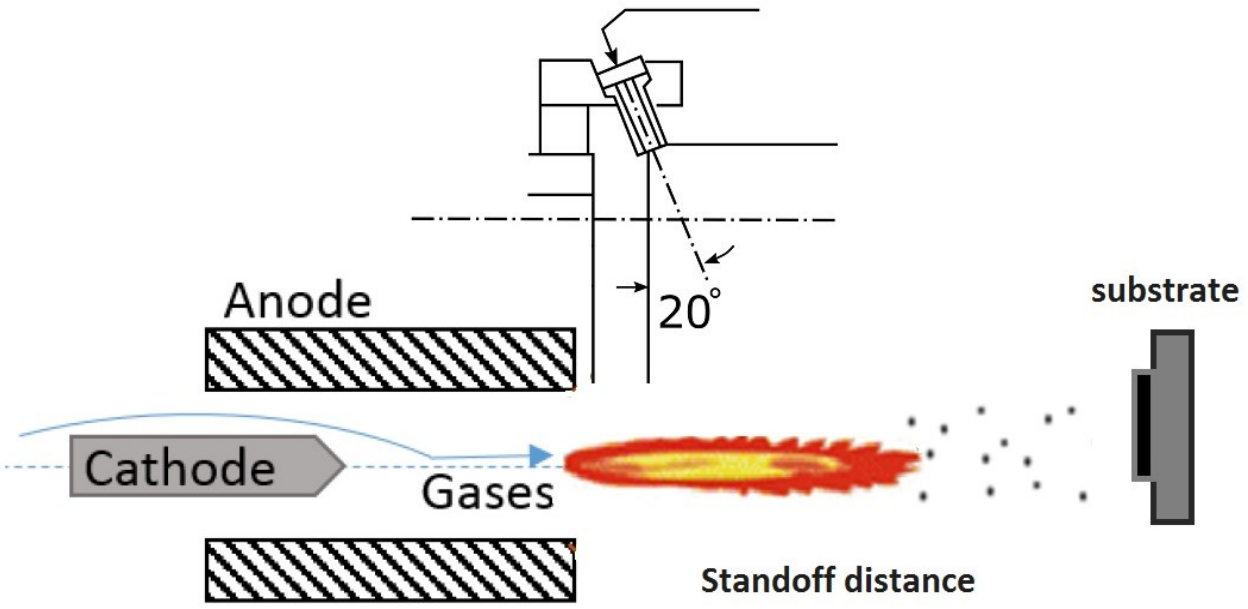

Figure 3-10. Schematic of the feedstock injection into the plasma gun

To evaluate the effect of coating method, two different coating conditions were also performed with HVOF. The HVOF process parameters used to spray the samples in this work are described in Table 3-5. As for spraying conditions, two oxygen/fuel ratios were used, but the combustion pressure kept constant. This condition allowed us to affect mainly the temperature of the spray particles as the combustion pressure is mostly linked to the in-flight velocity of the particles while the oxygen/fuel ratio is mainly related to the in-flight particle temperature.

Table 3-5. HVOF coating parameters

Parameters	High Oxygen/Fuel ratio	Low Oxygen/Fuel ratio
Standoff distance (cm)	25	25
Feed rate (g/min)	20	20
Oxygen flow rates (NLPM)	310	127
Fuel (propylene) rates (NLPM)	66	39
Air flow rates (NLPM)	422	352
Carrier gas (Nitrogen) (NLPM)	24	24
Oxygen pressure (psig)	150	150
Fuel Pressure (psig)	100	100

Air pressure (psig)	100	100

The spraying parameters were selected to reduce the temperature of the spray particles to preserve the GNP, minimize oxidation and create rough surfaces. A total number of 5 passes were deposited on each sample. The effect of each specific parameter on the coating microstructure will be discussed separately in detail in Chapter 4.

Before deposition, the grit-blasted substrates were ultrasonically cleaned in acetone. Then the substrates were pre-heated and/or air-cooled to ensure the temperature of the substrates remained in the range of 100 to 200°C during the deposition process. Moreover, a water-cooled substrate holder was utilized to reduce the substrate temperature. The substrate temperature was monitored during spraying with an Infrared Camera (FLIR Systems, USA).

To reduce the surface energy and also separate the effect of surface roughness on the wetting behaviour of the coatings, all samples were dipped into a 0.5 wt.% solution of stearic acid in 1-propanol and then dried [25]. A flat sample treated with stearic acid using the same method results in a contact angle of 98° and sliding does not take place on such a sample.

3.4. Coating characterization

The water contact angle of the coatings was measured using a sessile droplet method at room temperature of 21°C and 50% relative humidity. The setup comprises a digital camera (Nikon, Japan) a manual droplet generator and a backlight LED. (Figure 3-11). The image analysis and the measurements were performed using a code offered by Stalder et al. [70] as a plugin to the free image analysis software ImageJ (NIH, MD, USA). The measurements were repeated three times.

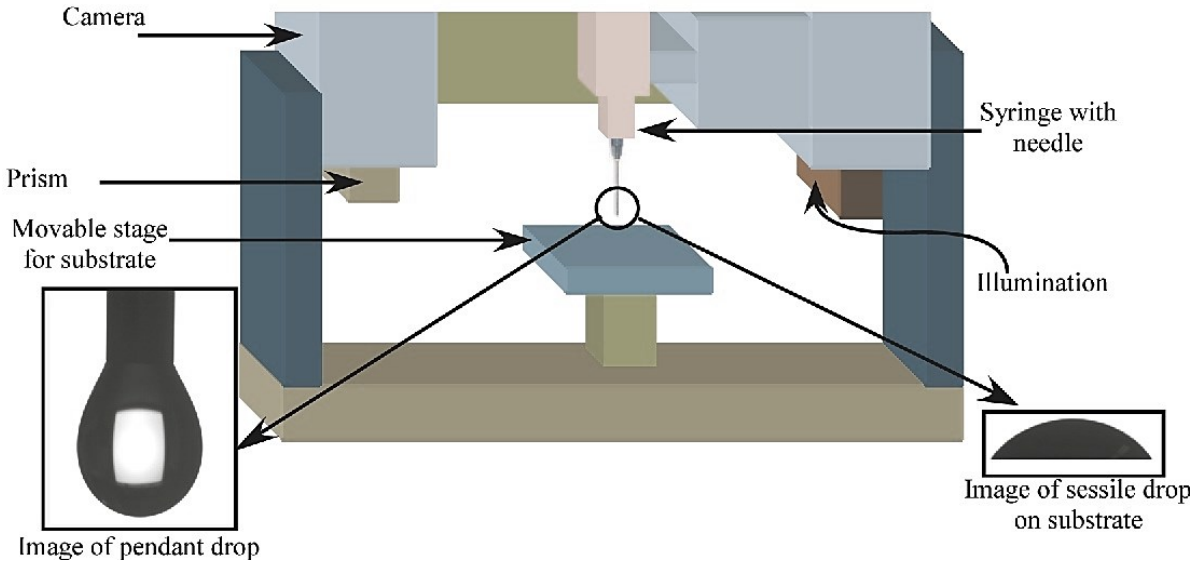

Figure 3-11. Schematic of the contact angle measurement setup[71]

To study the cross-sections of the coatings, the samples were cut using a precision cut-off machine (Secotom-15, Struers, Denmark) cold mounted in epoxy and then polished by standard metallographic procedures. The cut-off wheel used was 30A15 (aluminum oxide), selected according to the hardness of the material. The cutting program includes a rotational speed of 1500 rpm and a feed rate of the movable table at approximately 0.03 mm/s. Subsequently, the cleaned and dried sectioned samples were mounted in room-temperature curing resin. After curing, the mounted samples were polished in the Tegramin-25 polishing system to achieve a polished surface appropriate for metallurgical observations. The process started with wet grinding of the samples with 3 different grit silicon carbide grinding papers (320, 500 and 800). After grinding, additional polishing steps were performed to a final finish of 0.05 μm.

Once metallographic preparation was complete, an optical microscope was then used to study the cross-sections of the samples. In addition, the SEM microscope (Hitachi S-3400N, Japan) was used to take images from the surface and cross-section of the coatings to complete image analysis. The pictures recorded were taken with different magnifications. The image analyses of all the samples sprayed will be presented in Chapter 4. A 3-D Confocal Laser Scanning Microscope (CLSM) (LEXT-OLS4000, Olympus Corporation, Japan) was used for 3D topography imaging of the coatings and to measure the roughness of the coated samples. Raman spectrum was obtained

using a Renishaw InVia Confocal Raman microscope with 514 nm argon ion laser radiation and a diffraction grating of 1800 1/mm. The scan was performed using three 30 second exposures.

To study the corrosion resistance of the samples, polarization curves were obtained using a Stanford Research Systems EC 301where 0.1 M NaCl solutions were used as the electrolyte. This electrochemical analyzer is a three-electrode system with Ag/AgCl as a reference electrode and Pt wire as a counter electrode (Figure 3-12).

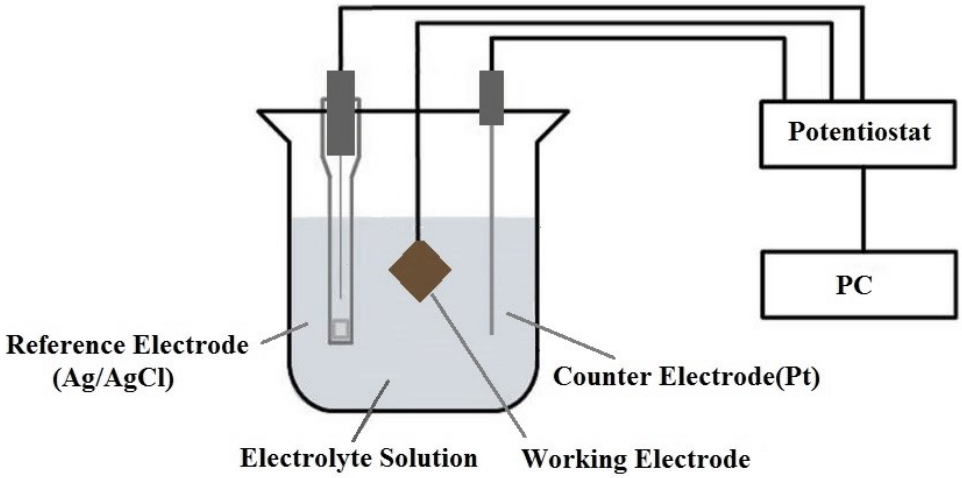

Figure 3-12. Schematic of the conventional three-electrode cell with a potentiostat

The sample acted as the working electrode with an exposed area of 1 cm^2 to the electrolyte at room temperature. Open circuit potential was monitored for 55 minutes to confirm its stability with time. The cathodic and anodic polarization measurement was performed from −0.4 to +0.2 V at a scan rate of 10 mV/s. The corrosion potential was determined by Tafel analysis from the resulting polarization curve. All the electrochemical tests were repeated three times to examine the repeatability of the results. Further analysis and the results of this work are described in the following chapter.

Chapter 4. Results and Discussion

As mentioned previously, the objective of this work was to investigate the effects of graphene nanoplatelets on the coating microstructure and its corrosion stability. This chapter will present the results after spraying the coatings, including wettability, water mobility, surface roughness as well as SEM analysis for APS and HVOF samples. Finally, the results of the Raman spectroscopy and corrosion resistance analysis of the optimized coated samples will be discussed.

4.1. Wettability, water mobility and roughness results

Table 4-1 shows the measured wettability and mobility parameters for all the APS and HVOF coated samples as well as the bare copper. The average surface roughness data (S_a) based on the confocal laser microscopy of the surfaces of the samples are also presented in Table 4-1. The average surface roughness of the sandblasted substrate was 1.8 μm. As illustrated in this Table, by coating the sample using thermal spray methods (APS and HVOF) following by stearic acid treatment, static contact angle values increased compared to the unsprayed substrate. The results are in agreement with another research by Wan et al. [72] that also reported that a superhydrophobic surface on Cu surface was produced by etching and hydrothermal treatment followed by stearic acid post-treatment and results showed a contact angle value of 157 °.

In order to investigate the effects of GNP in the coating, a comparison between the wettability and water mobility of Cu coatings and Cu-GNP coatings with the same coating parameters was performed. It should be mentioned that the feedstock particle size of the Cu-GNP is smaller than pure Cu because of ball-milling. In general, in the ball-milling process, cold-welding takes place, resulting in the agglomeration of the particles and an increase in particle size [73]. As pure copper is a ductile material and ball-milling would result in even larger particle size, this step was not performed. Although the pure Cu coating improved the wettability to some extent, the desired wettability and water mobility were not achieved by depositing the pristine copper as

indicated by the high sliding angle values that were observed. According to Table 4-1, the sliding angle and contact angle hysteresis decreased significantly in Cu-GNP coatings compared to when pure Cu powder was deposited. The relatively higher mobility of this composite coating shows that GNP has an effect on the surface chemistry and can be modified by stearic acid post-treatment to lower the surface energy and increase the hydrophobicity. This results could be linked with the findings of Han et al. who also modified graphene lipophilically with stearic acid: their results showed a good reaction and affinity between graphene and stearic acid [74]. Also, the high stability of superhydrophobic coatings created from graphene-containing materials on copper alloy by other researchers [75] confirms the effective contribution of graphene on producing superhydrophobic surfaces.

Table 4-1. Wettability, Water mobility and roughness results for the APS and HVOF samples.

The numbers after "±" sign are standard deviation values.

Sample	Contact angle (CA°)	Sliding angle (SA°)	Contact angle hysteresis (CAH °)	Average surface roughness (S_a) – μm
Bare Cu	102 ± 2	No Sliding	>20	0.5
Cu-S	98 ± 3	No Sliding	>20	0.5
Cu-LP-APS-S	Poor deposition	-	-	-
Cu-MP-APS-S	130 ± 3	10	12	13
Cu-HP-APS-S	115 ± 3	>20	13	11
Cu-GNP-LP-APS-S	Poor deposition	-	-	-
Cu-GNP-MP-APS-S	152 ± 2	8	7	12
Cu-GNP-HP-APS-S	140 ± 3	12	10	10
Cu-LR-HVOF-S	135± 1	>20	14	9
Cu-HR-HVOF-S	110± 1	> 20	20	7
Cu-GNP-LR-HVOF-S	164 ± 1	<1	3	10
Cu-GNP-HR-HVOF-S	122 ± 1	14	12	8

As expressed earlier, the process parameters can potentially have a significant effect on the wetting behaviour of the coatings. As Table 4-1 shows, the APS coated samples with a plasma power of 25 kW (MP) showed relatively better results in water repellency and water mobility compared to the other spray parameters. The wettability results showed that a small variation of the spraying parameters could significantly affect the structure of the coating. The best results using APS regarding wettability and water mobility were achieved by adjusting the hydrogen flow rates and thus reducing the process temperature in the Cu-GNP-MP-APS-S sample. Moreover, the desired morphology was achieved and more GNP was maintained which resulted in the highest contact angle, the lowest sliding angle and contact angle hysteresis.

In addition, in HVOF with the lower oxygen-fuel ratio, a higher contact angle and a lower sliding angle, which are an indication of a superhydrophobic surface, were attained. The reasons for such characteristics of the coatings are further discussed in section 4.2. The best APS and HVOF samples exhibited water contact angles above 150° which is the first requirement for a superhydrophobic surface. Nevertheless, the Cu-GNP coated samples which were sprayed by the HVOF process exhibited a larger contact angle compared to the APS process, indicating a high water repellency. Also, the sliding angle and contact angle hysteresis were lower, representing better water mobility.

Therefore, it can be concluded that the Cu-GNP coatings produced by these surface engineering processes (APS and HVOF) increased the contact angle values and decreased the sliding angle. The Cu-GNP coating formed with the lower temperature HVOF process exhibited better results compared to the coated samples by APS with optimum parameters. Also, a smaller standard deviation of contact angle values of HVOF-coated samples indicates more homogeneous coatings compared to the APS-coated samples. This can be principally related to the higher velocity of the particles injected during the HVOF process.

According to Table 4-1, the average surface roughness data (S_a) of APS coatings showed relatively higher values (Sa) while the HVOF coated samples exhibited the lower surface roughness. The smaller amount of roughness in HVOF coated samples is attributed to the higher velocity of the particles compared to the APS process. A comparison of the surface roughness of APS coated samples results showed lower plasma power leads to the more roughness on the surface. Moreover when comparing the HVOF surface roughness results it can be concluded that

by decreasing the oxygen to fuel ratio, the roughness of the samples sprayed by HVOF increased slightly. This can be attributed to the lower temperature with applying a lower amount of fuel to the process.

Furthermore, Cu-GNP coated samples using HVOF and APS have surface roughness (S_a) values which are lower than those of the Cu coated samples. This could be attributed to the larger particle size of the copper feedstock. With the Wenzel wetting model, it is expected to have higher contact angle values when increasing the roughness and this model indicates that surface roughness has an amplifying effect on the water contact angle of a surface. However, from the surface roughness and the wettability results in this work, it can be concluded that the Wenzel model is not sufficient to describe the correlation between the wettability and the surface roughness. Although the roughness characteristics of a surface cannot be fully described with a single number (Sa), the Cassie-Baxter model might partially explain the correlation between the wettability and surface roughness in this case. Furthermore, wettability and water mobility is a complex phenomenon and cannot be described with a single parameter. As mentioned in previous chapters, both the chemistry and the morphology have major affect on the wettability.

Figure 4-2 illustrates the CLSM 3D surface topographies of the coated samples of scanned surface areas of about 1800×1800 μm^2. The results indicated that the APS coated samples showed more roughness while the HVOF coated samples exhibit lower surface roughness. The images also demonstrate that the surface peaks are more uniformly distributed in the HVOF coatings compared to those deposited with the APS method. It is evident from the literature [76] that the APS process results in higher porosity coatings compared to HVOF. Consequently, a rougher surface is achieved with APS.

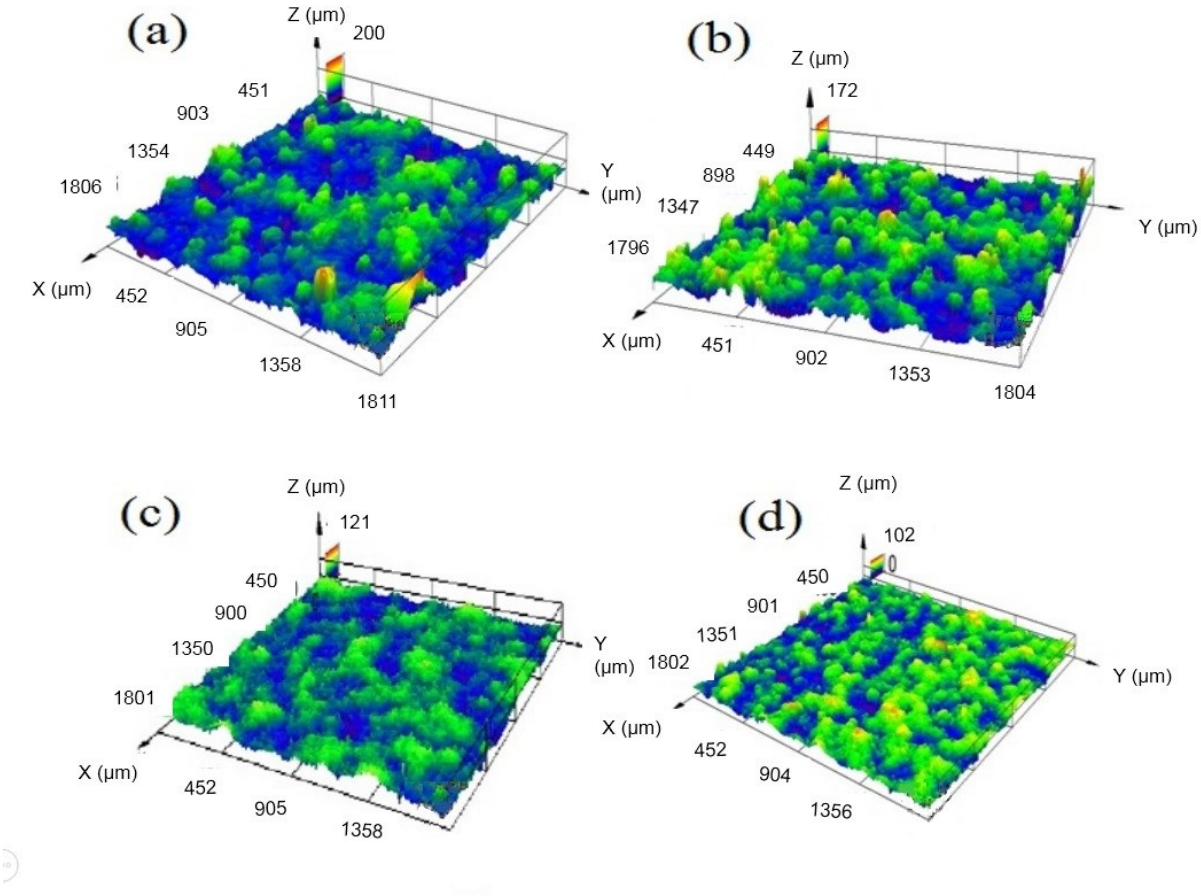

Figure 4-1. CLSM top surface topography of the coated samples: (a) Cu-GNP-HP-APS-S, (b) Cu-GNP-MP-APS-S, (c) Cu-GNP-LR-HVOF-S, and (d) Cu-GNP-HR-HVOF-S

4.2. Morphological studies

4.2.1. APS coated samples

SEM micrographs of APS coated samples can be seen in Figures 4-2 to 4-7. The images show that the stearic acid treatment has not meaningfully changed the morphology of the coatings. This fact proposes that the difference in the morphology of the coatings plays an important role to have a different wetting and water mobility characteristic.

4.2.2. Copper coatings by APS

As mentioned before, an SEM micrograph of the Cu-HP-APS-S coating is presented in Figure 4-2. This coating shows hydrophobicity. However, the sliding angle is not low enough to have the desired water mobility on the surface. The spray particles' state was verified by splat observation. In this coating, particles with comparatively high plasma power and consequently high temperature impacted on the substrate. As is shown in the image, the high temperature of the impacting particles caused them to splash. Moreover, the size of splats is larger in this coating compared to the other coatings and splats overlapped on their edges. The surface roughness is erratic in this coating.

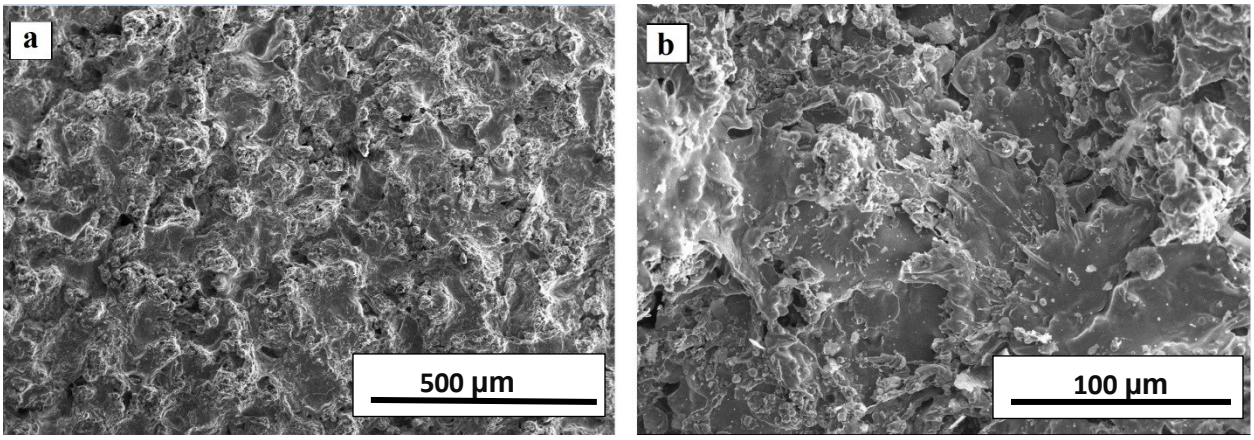

Figure 4-2. SEM micrographs of the Cu-HP-APS-S sample with relatively high plasma power

The surface morphology of the Cu-MP-APS-S coating is shown in Figure 4-3. Due to the medium plasma power, the surface morphology of this coating includes smaller size of splats when compared to the high power. Also, partially melted particles can be observed in the coating morphology. The temperature of the particles was lower than the Cu-HP-APS-S coating hence more viscous and less mobile which leads to less molten particle splashing. The pancake-shaped splats are visible in this morphology. This coating showed a high water contact angle compared to the other coatings due to its morphology and specific roughness features. Similarly in other studies, these features are reported to improve hydrophobicity [10].

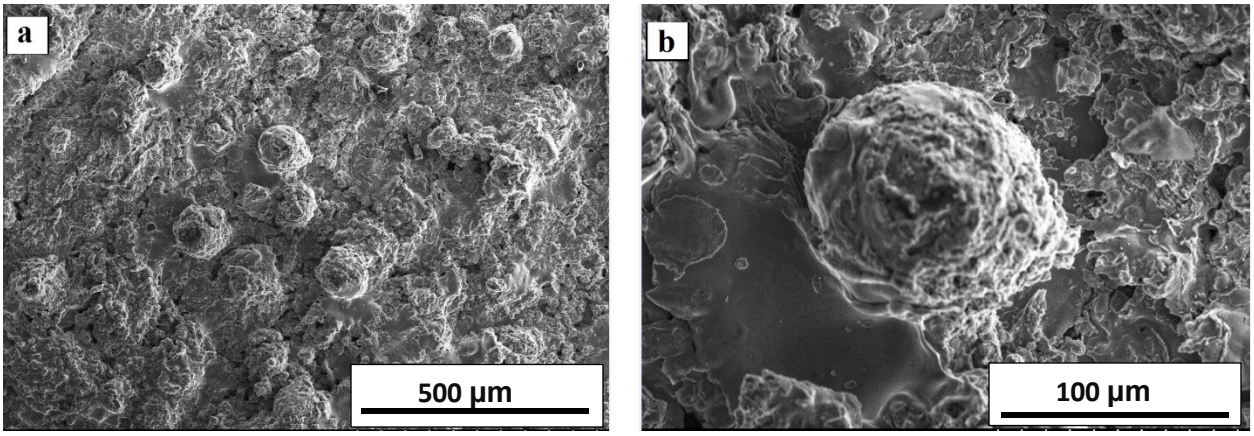

Figure 4-3. SEM micrographs of the Cu-MP-APS-S sample with medium plasma power

Figure 4-4 shows the top surface of Cu-LP-APS-S sample. This coating was formed with the lowest hydrogen flow rate and thus lowest plasma power in this work. As a result, this coating was not well attached to the substrate owing to the low plasma power. It can be seen in this coating microstructure that the presence of the spherical particles is evident and this coating has less erratic roughness features. The same observation is reported by Sharifi et al. when the temperature and velocity of the particles are very low [7].

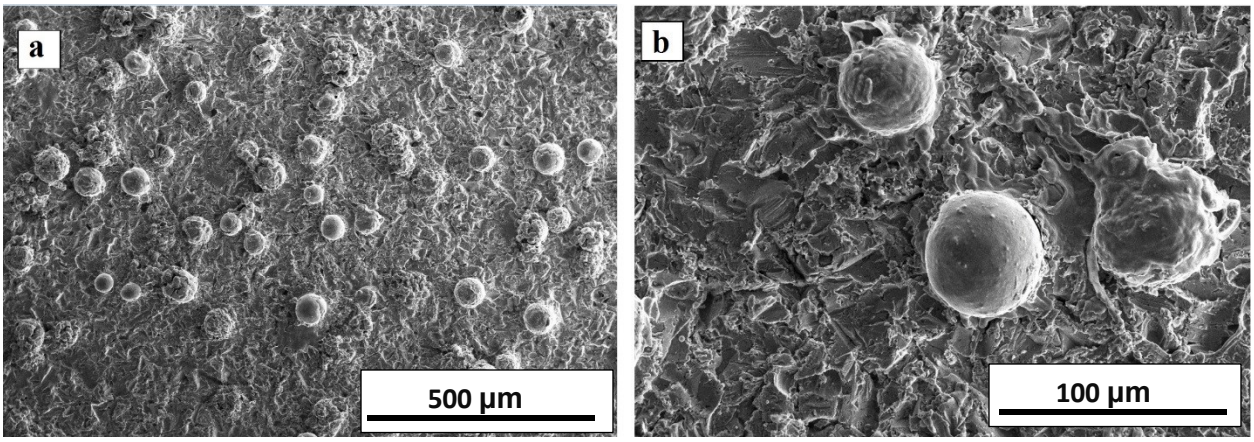

Figure 4-4. SEM micrographs of the Cu-LP-APS-S sample with relatively low plasma power

With a low plasma power, the coating did not adhere well to the substrate. Accordingly, to compare the morphology of the APS coated samples containing GNP further image analysis was only performed for the samples with medium and high plasma power.

4.2.3. Copper-GNP coatings by APS

SEM micrographs of the coatings sprayed with medium and high plasma powers are shown in Figure 4-5 (a, b, c and d), respectively.

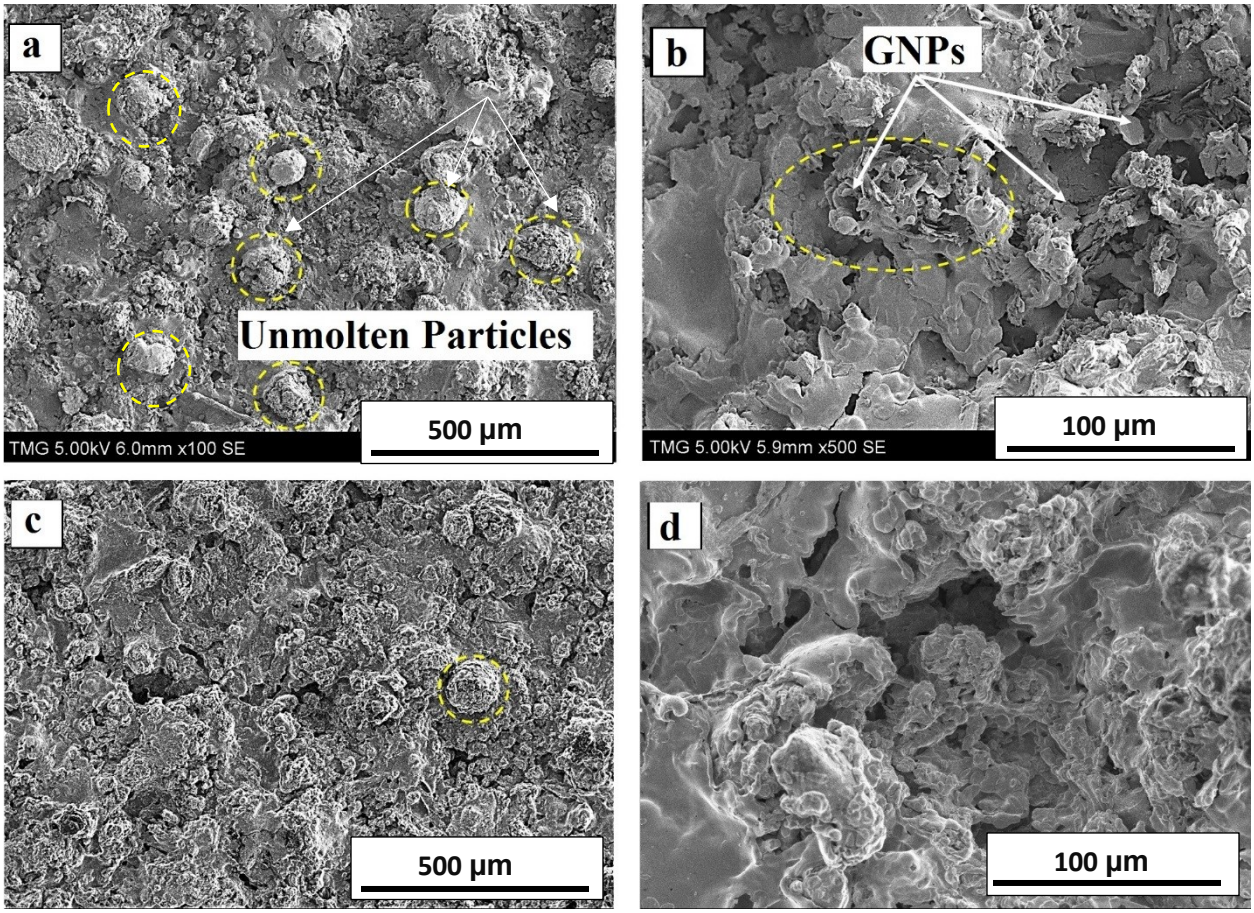

Figure 4-5 SEM micrographs of the Cu-GNP-MP-APS-S (a and b) and Cu-GNP-HP-APS-S (c and d) samples

When comparing the surface morphology of the two samples, it can be seen that the surface morphology of the APS coated sample with medium power (Figure 4-5 a) has more irregularities compared to the sample sprayed with high plasma power (Figure 4-5 c). It can be seen that the microstructure of the Cu-GNP-MP-APS-S coating is formed by a combination of flattened splats and partially molten particles. By decreasing the hydrogen flow rate and plasma power, the temperature of the particles was relatively lower thus less splashing. Lee et al. [77] also reported that when the H_2 amount is very low in the plasma, it not only decreases the particle temperature

but also decreases the tendency for any in-flight reduction. Lower average particle temperatures indicates that some of the particles are expected to remain unmolten and preserved as such in the deposition process.

One of the exciting features of this coating is the spherical flower shape features that represents a hierarchical surface and are the desired morphology for a superhydrophobic surface. This kind of hierarchical hybrid structure was also reported by other researchers and suggested to be beneficial to the biological performance of the coating [65]. By the reinforcement of GPs, the wear properties of the composite coating were improved. Moreover, in vivo experiments proved that the composite coating demonstrated also good biocompatibility compared to pure calcium silicate coating. The implant showed enhanced bone-implant contact ratio for composite coating after 3 months' implantation. These structural flower shape features are seen to be more numerous on the surface of the Cu-GNP-MP-APS-S coating that were sprayed with medium plasma power compared to those sprayed at the high plasma power applied. Due to the lower plasma power and consequently cooler deposition conditions, the semi-molten particles impacting onto the substrate will result in these features. The high water contact angle of this coating compared to the other coatings is attributed to its microstructure and roughness features. Also, this sample shows the lowest sliding angle among all the APS samples.

Comparing Figures 4-5 (b) and (d), graphene nanoplatelets can be easily seen in the sample sprayed at medium power (b). On the other hand, in the Cu-GNP-HP-APS-S coating (d), the plasma power is higher and particles with higher temperature impacted onto the substrate. Due to the higher plasma power and consequently higher particle temperature, fully molten particles and large splats can be observed on the top surface of this coating. It is difficult to identify GNP in this image and this could be attributed to the higher plasma power and temperatures that may cause graphene combustion.

In a similar study, Kang et al. [78] investigated the role of spray parameters on microstructural properties of multi-walled, carbon nanotube-reinforced, Cu-composite coatings. Their findings showed that the microstructure of the pure Cu coating included melted splats, un-melted particles and further oxide layers. The coating formed a lamellar structure which is the result of rapid cooling of melted splats followed by solidification. The shrinkage had caused inter-lamellar void formation.

Figure 4-6 shows the cross-sectional backscattered electron (BSE) of these two samples (medium and high power APS). The cross-sectional view of both coated samples show that the deposited layers covered the substrate equally well. Splats are also visible in the coating layers. Interlamellar pores can be mostly observed in the cross-sectional image. The smaller water contact angle of Cu-GNP-HP-APS-S compared to Cu-GNP-MP-APS-S coating can be attributed to these relatively larger troughs between roughness features. In another study, Sharifi et al. [13] revealed that a smaller contact angle can be associated to larger gaps between roughness features.

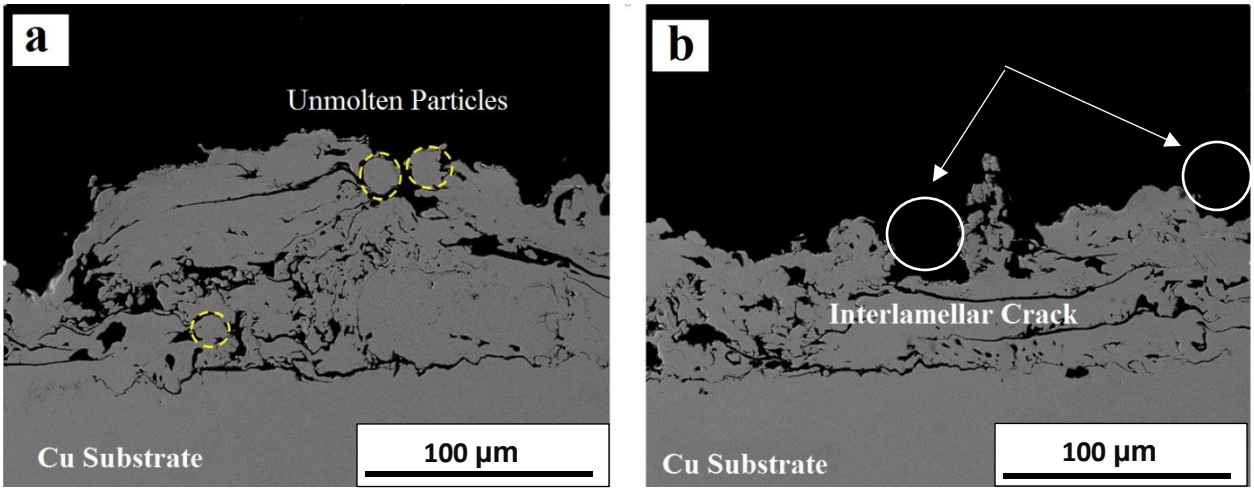

Figure 4-6.SEM micrographs of cross-sectional view of the Cu-GNP-MP-APS-S (a) and Cu-GNP-HP-APS-S (b) samples

The Cu-GNP-MP-APS-S sample at low thermal energy condition (with a plasma power of 25 kW) shows a more porous microstructure compared to those sprayed at a higher temperature. Furthermore, SEM images illustrate a typical lamellar appearance and porosities within/between flattened splats are observable. Because of the formation of semi-molten particles, a comparatively more irregular morphology has been formed as shown in Figure 4-6 (a), and subsequently higher contact angle values were achieved compared to Cu-GNP-HP-APS-S.

Characteristically, H_2 gives higher enthalpy to the plasma and consequently, higher particle temperatures which in general should produce higher density depositions. The particles in the high temperature environment will be fully melted and quickly solidify which changes their volume and temperature [77].

Energy Dispersive X-ray (EDX) elemental distribution of a Cu-GNP-MP-APS-S sample was performed to identify carbon, and therefore GNP, given the fact that no other carbon sources

were present in the structure of the coating. The analysis point is shown in Figure 4-7. The results are presented in Table 4-2.

Figure 4-7.SEM Image and elemental mapping of the Cu-GNP-MP-APS-S sample

Table 4-2. Elemental distribution of Cu-GNP-MP-APS-S coating

Element	Weight %	Atomic %
C K	55.82	85.23
O K	2.36	2.70
Cu L	41.83	12.07
Totals	100.00	

In summary, it can be concluded that the Cu-GNP APS coatings that can be produced by controlling the deposition parameters have a surface morphology that will encourage non-wetting

behaviour and hydrophobicity. Water contact angles as high as 152° were achieved. Moreover, the intrinsic hydrophobic properties of graphene aided the superhydrophobicity of the surfaces in the samples in which graphene was preserved by optimizing the coating process. According to the results of previous studies [25], it can be concluded that by decreasing the temperature to the lowest possible value, a lower wettability of the coatings may be produced. However, according to the high sliding angle values achieved in this study, it can be determined that the APS coatings do not provide the required water mobility. This might be due to the non-uniform morphological features formed by the APS process and its unpredictable pattern. The obtained results in this study suggest the importance of using a coating method that brings to the coating surface a fine and consistent texture and morphology.

4.2.4. HVOF coated samples

4.2.4.1. Copper coatings by HVOF

Figures 4-8 (a) and (b) show SEM images of the top surface of the Cu coating deposited with HVOF at high and low oxygen-to-fuel ratios, respectively. In HVOF, particles impact against the substrate in a molten or semi-molten state to form coatings [79]. The presence of unmolten particles in a matrix of partially and fully molten particles is more visible on the top surface of the Cu-LR-HVOF-S (Figure 4-8b) coating compared to the same coating with higher oxygen to fuel ratio (Figure 4-8a). Some spherical shapes of the deposited particles can be seen in the microstructure of this coating. This could be related to the lower temperature and velocity of the in-flight particles. The selected parameters of operating conditions are lower than of a typical HVOF gun. Since the as-received Cu powder deposited in this coating is in the range of 60-70 μm, it can be concluded that the particles that are larger in diameter could not melt under this spraying condition.

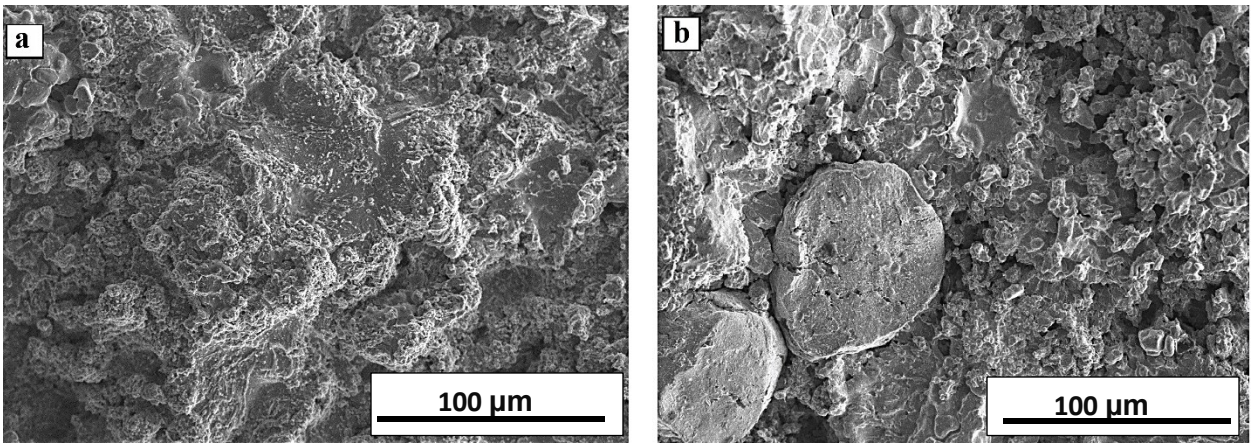

Figure 4-8. SEM micrographs of the (a) Cu-HR-HVOF-S and (b) Cu-LR-HVOF-S samples

4.2.4.2. Copper-GNP coatings by HVOF

Figure 4-9 shows the top surface SEM image of the Cu-GNP coating deposited with low oxygen-to-fuel ratio HVOF. The morphology shows graphene nanoplatelets could be maintained in the structure and the presence of unmelted particles is evident in the morphology of this coating. It can be seen in Figure 4-9 that the GNPs were preserved and embedded in the Cu matrix. Additionally, the HVOF coating shows a hierarchical structure. Compactness of sprayed particles is one of the main properties for HVOF coatings and usually improves their performance in application such as anticorrosion coatings [79].

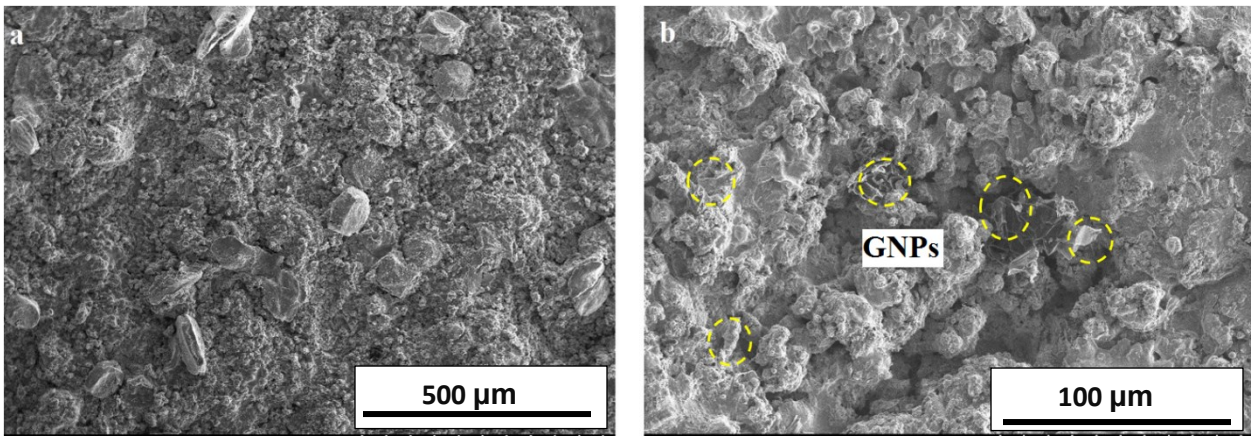

Figure 4-9. SEM micrographs of the Cu-GNP-LR-HVOF-S with relatively low Oxy/Fuel ratio

The substrate measured temperature was 50 °C for the first pass and 80 °C for the last pass during the HVOF process comparing to APS process which was 100°C and 220 °C, respectively. This relatively low substrate temperature results in less oxidation of the coating because of the rapid cooling rate of the deposited particles. For this coating, due to the low gas temperature, it is expected that more graphene will be preserved. The achieved morphology results in a higher contact angle value of 164° and the desired water mobility revealed through a water sliding angle of less than 1°.

The top view SEM micrographs of the Cu-GNP coating samples with relatively high oxygen-to-fuel ratio are displayed in Figure 4-10. In this coating, the micrograph displays a dense microstructure with high consistency and no surface cracks. Furthermore, few porous areas can be seen in the microstructure of this coating. The amount of unmolten and partially molten particles is less in this coating morphology.

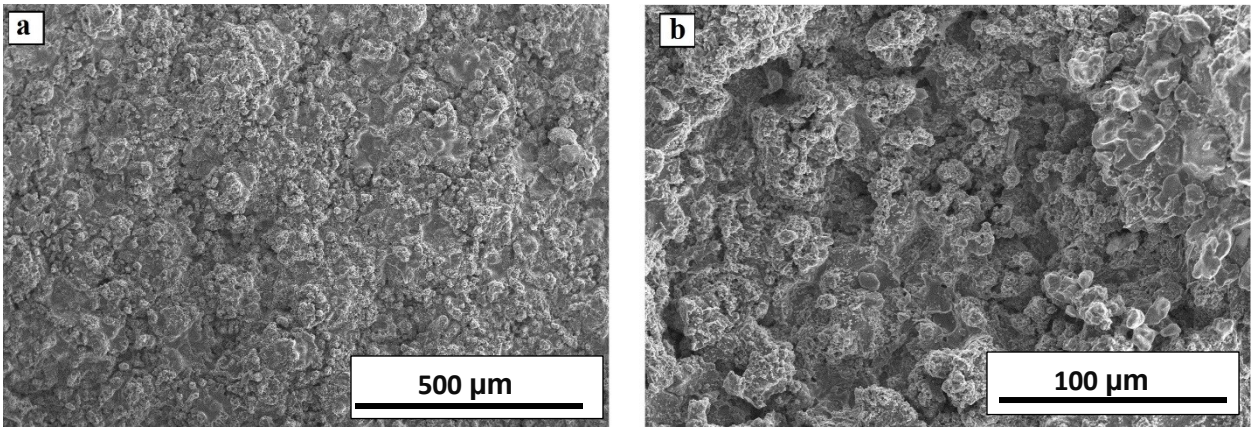

Figure 4-10. SEM micrographs of the Cu-GNP-HR-HVOF-S with relatively high Oxy/Fuel ratio

The temperature measurement of the in-flight particles was not possible in these coatings due to the very low temperature of the process. In order to compare the two sets of coating parameters, the oxygen-to-fuel ratio was calculated and compared with the stochiometric ratio. The combustion reaction of propylene is:

$$C_3H_6 + \frac{9}{2}O_2 \rightarrow 3CO_2 + 3H_2O \quad \Delta H_c = -2077\ kJ/mol \qquad \text{Eq. (4.1)}$$

Therefore, the stoichiometric O/F ratio is ${}^{O}/_{F_{stoichiometric}} = {}^{9}/_{2} = 4.5$

Density of propylene $\rho_{C_3H_6} = 1.81\ kg/m^3$ and its molar mass $M_{C_3H_6} = 42.08\ g/mol$

$$n_{C_3H_6}\left(\frac{mols}{s}\right) = \frac{\rho_{C_3H_6}\cdot(SCFH)_{C_3H_6}\cdot 7.866\times10^{-6}}{M_{C_3H_6}} = 3.38\times10^{-4}\times(SCFH)_{C_3H_6} \quad \text{Eq. (4.2)}$$

$$n_{O_2}\left(\frac{mols}{s}\right) = \frac{\rho_{O_2}\cdot(SCFH)_{O_2}\cdot 7.866\times10^{-6}}{M_{O_2}} = 3.51\times10^{-4}\times(SCFH)_{O_2} \quad \text{Eq. (4.3)}$$

$$O/_F = \frac{n_{O_2}}{n_{C_3H_6}} = 1.038\times\frac{(SCFH)_{O_2}}{(SCFH)_{C_3H_6}} \quad \text{Eq. (4.4)}$$

$$\overline{O/_F} = \frac{O/_F}{O/_{F_{stoichiometric}}} = 0.23\times\frac{(SCFH)_{O_2}}{(SCFH)_{C_3H_6}} \quad \text{Eq. (4.5)}$$

In this work the calculated high oxygen to fuel ratio is $\overline{O/_F} = 0.33$ which represents a richness ratio (R) of 3.03 while the calculated low oxygen to fuel ratio is $\overline{O/_F} = 0.23$ which gives a richness ratio (R) of 4.34. According to the literature, the temperature is significantly lower than the temperature of combustion [80]. When the oxygen to fuel ratio is in stoichiometry, the high gun temperature results in high particle temperature (Figure 4-11). In this work, the oxygen-to-fuel ratio is lower than stoichiometry, hence varying the ratio results in a change in process temperature. It can be concluded that the lower oxygen-to-fuel ratio used herein results in lower temperatures and increases the possibility of maintaining GNPs, as confirmed by the SEM images in Figure 4-9.

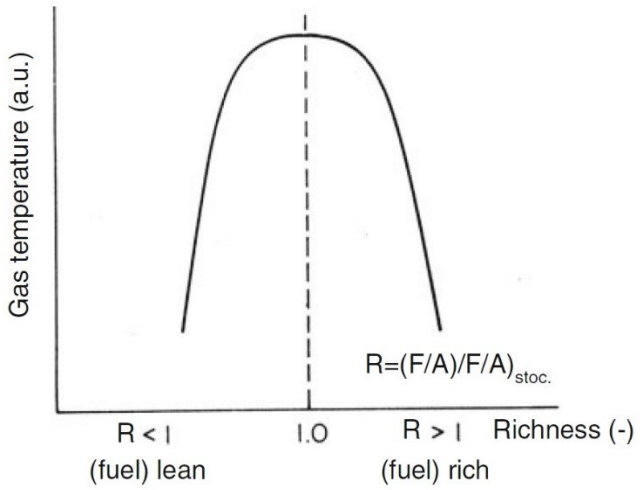

Figure 4-11.Variation of combustion temperature with richness ratio [80].

The cross-sectional view of these two coatings are presented in Figures 4-12 (a) and (b). It can be seen that the coating is well adherent to the substrate and the amount of porosity observed in the morphology is small. The interface between the substrate and the coating can be distinguished. In the cross-section image of the Cu-GNP-LR-HVOF-S sample (Figure 4-12(b)), the presence of unmolten particles can be seen.

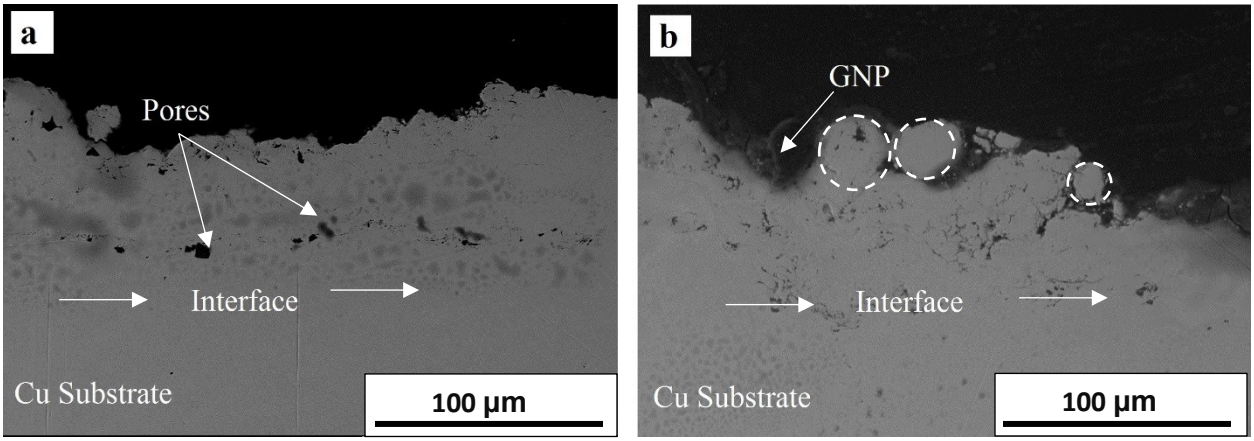

Figure 4-12. Cross-sectional view SEM micrographs of the Cu-GNP-HR-HVOF-S (a) the Cu-GNP-LR-HVOF-S (b). The arrows point to the interface to the substrate material.

4.2.5. Microstructural Comparison of plasma-sprayed vs. HVOF coatings

Figure 4-13 (a) displays a cross-section of a plasma-coated sample. In this image, the plasma-sprayed coating contained many pores of different shapes and sizes. Unlike the HVOF spray coating in Figure 4-13 (b), the splat boundaries are clear. The HVOF coated sample had a denser structure compared to the APS samples. This denser coating was achieved due to the higher velocity of the particles in this process. Also, the microstructure of the HVOF coatings is more homogeneous when compared to the APS coatings; the HVOF-sprayed particles are less flattened and less oxidized due to the effect of the coating particles' high speed. This leads to highly consistent strength of splats. In APS coating, the interlamellar pores are easily visible. The reason is not well known but likely related to gas trapped between splats. In HVOF these interlamellar pores are usually absent due to the higher impact velocity of the particles. Relatively homogenous coatings are critical for improving the corrosion resistance of the coatings which is also affected by the porosity. In a comparison study performed by other researchers, the oxygen content of the APS coatings was reported to be almost double the amount of the HVOF sprayed coatings due to the presence of small pores between the stacked particles [81]. In the HVOF process, the feedstock includes finer particles, which generates a finer morphology. Consequently, a more consistent coating microstructure can be produced compared to the APS samples.

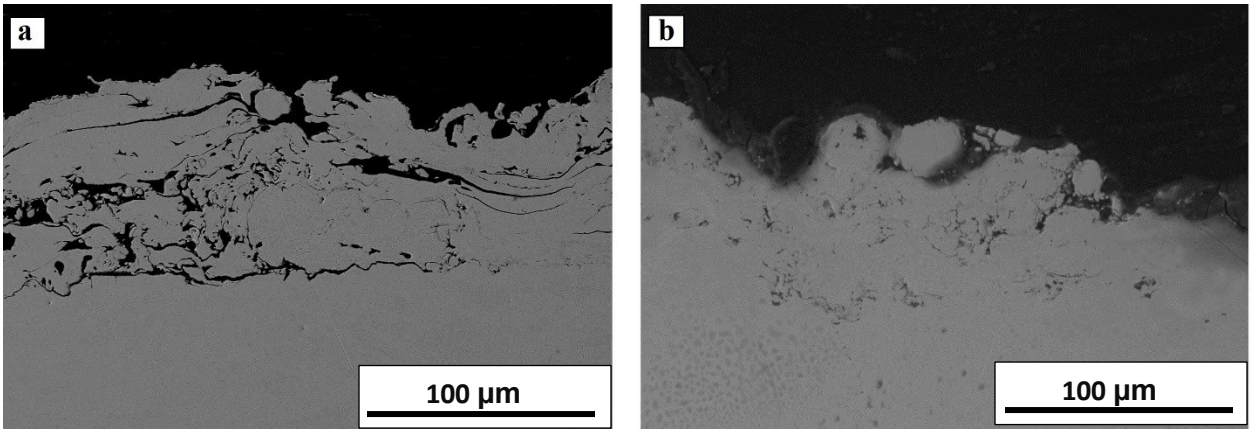

Figure 4-13 SEM Cross-sectional micrographs of the Cu-GNP-MP-APS-S (a) and Cu-GNP-LR-HVOF-S (b) samples

4.3. Raman spectroscopy

In order to further detect and confirm the presence of GNP in the coatings, as well as to determine the potential effect of thermal spraying on the structural properties of the GNP in the coating, Raman spectroscopy was performed in this study.

Three spectroscopic features represent the Raman spectrum of GNP. The G peak observed at 1580 cm^{-1} is attributed to the bond stretching of all pairs of sp^2 atoms in chains and rings, the D peak at 1350 cm^{-1} characterizes the breathing modes of six-atom rings and the 2D peak which shows the second order of the D band at ~2700 cm^{-1}. The G and D peaks in the Raman spectra are a direct indication of the existence of carbon materials [65]. From the Raman spectra presented in Figure 4-14, D and G peaks confirmed the retention of carbon material in the plasma sprayed coating. The D peak intensity indicates the number of defects in the carbon material. Increased D peak intensity means increased defect density and edges [68].

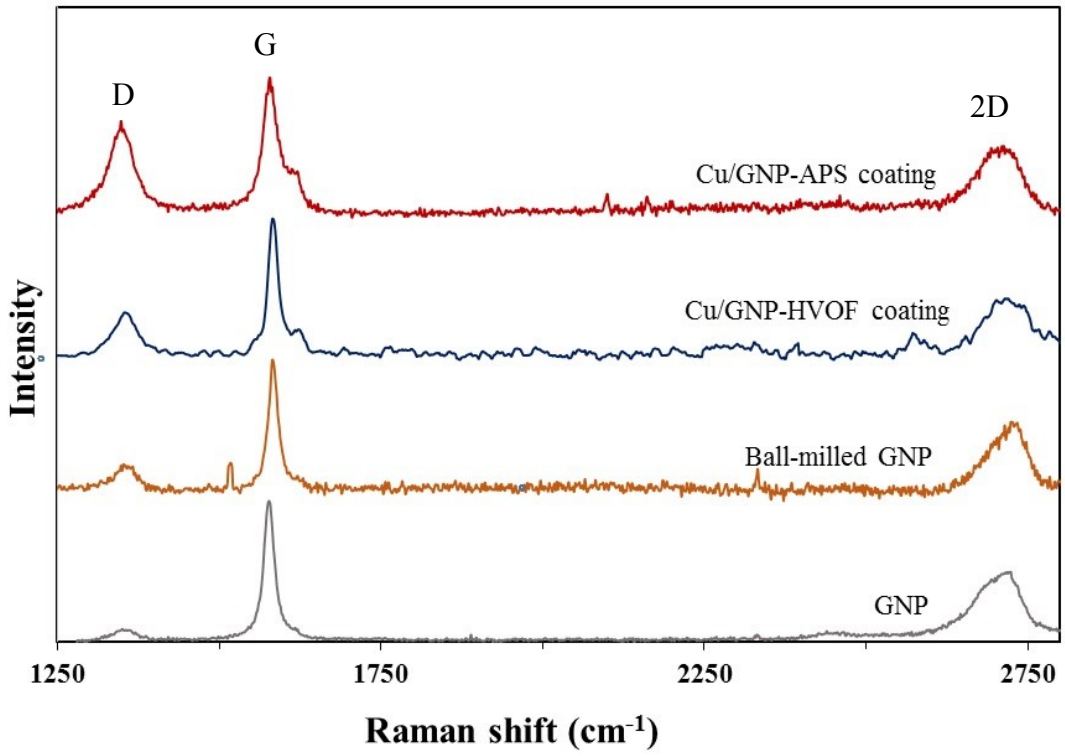

Figure 4-14. Mean Raman spectra of the unprocessed GNP, ball-milled GNP with Cu before spraying, HVOF and APS sprayed coatings containing GNP.

Figure 4-14 clearly demonstrates the differences in structural ordering in the GNP: the D peak intensity increased significantly in the plasma sprayed coating compared to the unprocessed GNP, which indicates that the defects increased after the plasma spraying process. However, the intensity of the D peak in HVOF sample has not increased as much. It may be attributed to the lower temperature of HVOF compared to the APS process. An increased ratio of D and G band intensities (I_D/ I_G) from ~0.1 to ~ 0.4 for HVOF and from ~0.1 to ~0.6 were observed for the GNP (Figure 4-15). The obtained results correspond to the reduction in distance between defects which indicates the formation of additional defects in the GNP structure. It is important to note that an utterly disordered graphene layer may have an I_D/ I_G ratio of more than 3 [82]. However, there is no significant change in the intensity, position or width of the 2D band followed by thermal spraying, which demonstrates that this procedure does not change the number and orientation of graphitic layers in the GNP structure. Therefore, although there has been some increase in the disorder in the structure, the intrinsic structural integrity of GNP can be well maintained in the coating process.

The comparison of the mean Raman spectra of the as-received GNP and ball-milled GNP showed there is some increase but that this difference was not majorly significant. As mentioned before, with a controlled ball-milling including an appropriate duration and method to achieve a uniform dispersion of GNP in the copper matrix, the structural damage can be reduced. It is also observed previously by Yue et al. [83] that 3 hours of milling does not change the amount of defects significantly. However, the slight increase in the amount of I_D/I_G ratio of milled GNP is related to cold welding and fracturing actions of the ball milling process [84].

On the other hand, thermal spraying results in considerable differences in the structural ordering within the GNP, as has also been reported in similar studies on alumina-graphene nanocomposite coatings by HVOF [63]. In this study, they described that when the feedstock is passed in a combustion chamber containing a combusted fuel at high temperatures, the I_D/I_G ratio of the GNP increases after spraying.

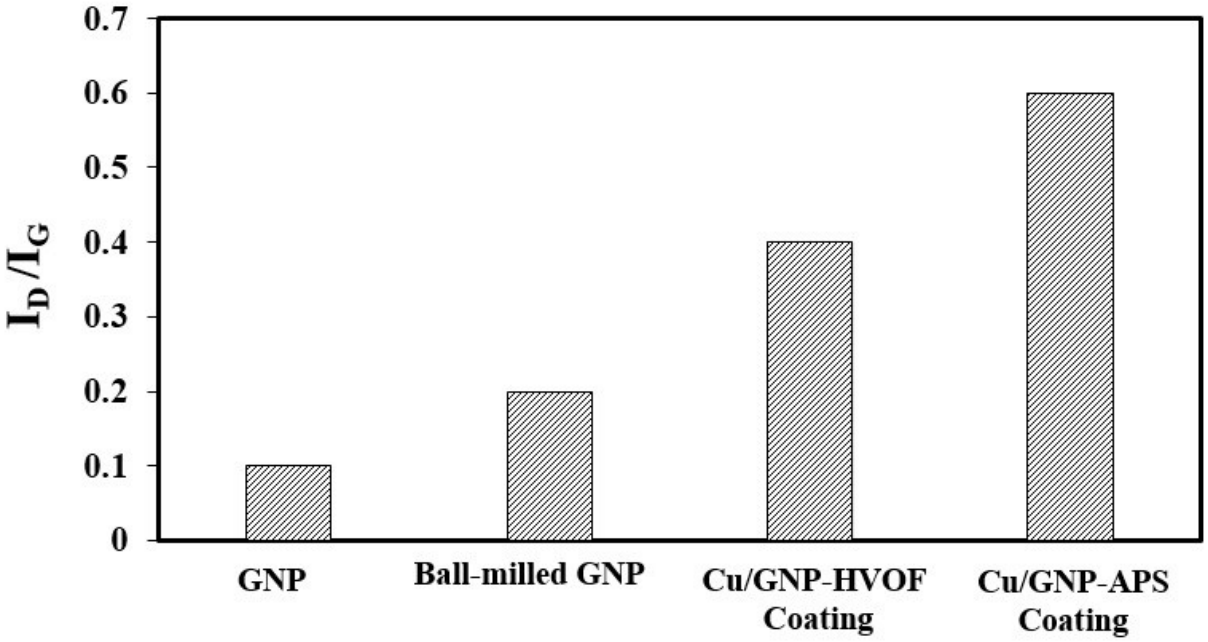

Figure 4-15. The distribution of I_D/I_G of pure GNP, ball-milled GNP, the HVOF and the APS sprayed samples

4.4. Potentiodynamic polarization analysis

With the provided set up, the open circuit potential was recorded for 55 minutes for bare copper, the Cu coating and the best Cu-GNP coating on Cu substrates in order to get a stable potential with time before running the corrosion tests. Potentiodynamic polarization plots are shown in Figures 4-16 to 4-18. Polarization curves were used to indicate the corrosion rates of Cu and Cu-coated samples. Figure 4-16 shows the Tafel polarization curves of the Cu and Cu-coated samples with APS. The corrosion potential (E_{corr}) of the Cu-GNP coated sample, which is the intercepts of the anodic and cathodic regions of the plot, is 37 mV more positive compared to the bare Cu. The shift in E_{corr} with a more positive direction demonstrates that coatings can inhibit the corrosion of Cu, which illustrates the high corrosion resistance of the coatings. However, Cu-MP-APS-S sample which do not have GNP in the structure of the coating did not show any significant difference in its corrosion potential (E_{corr}).

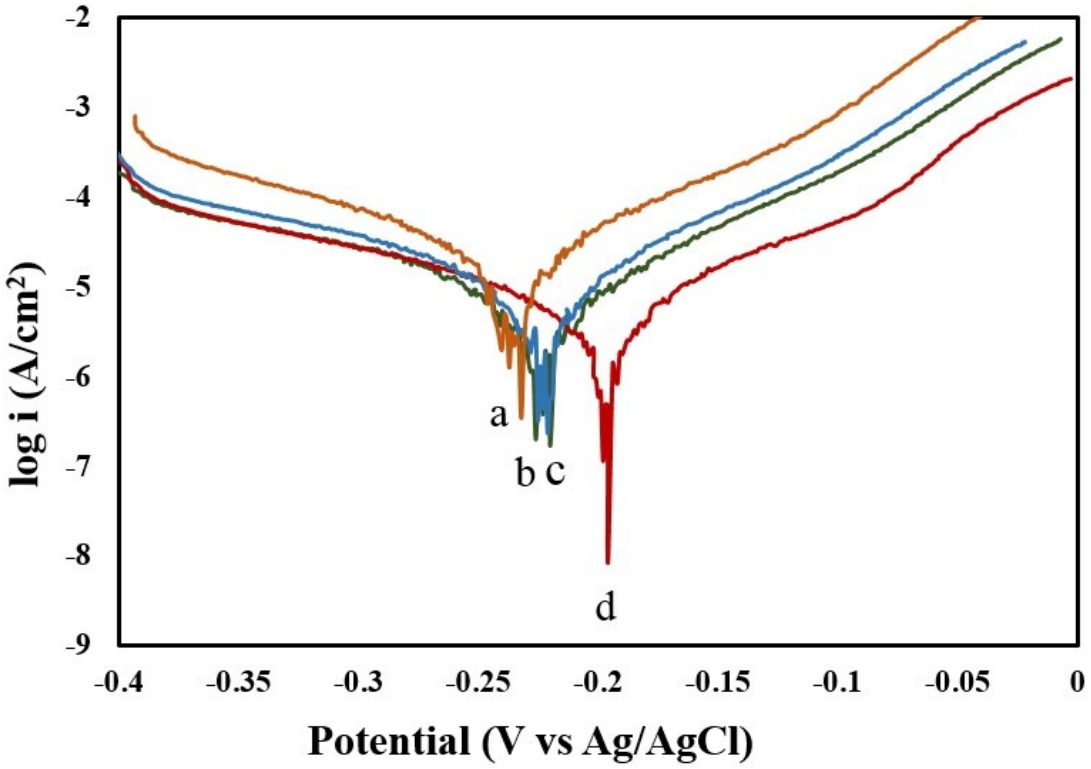

Figure 4-16. Tafel polarization curves of a) bare Cu, b) Cu-S c) Cu-MP-APS-S and d) Cu-GNP-MP-APS-S

As can be seen in the graph, the anodic current densities of the graphene-coated samples are lower than the uncoated samples signifying that the graphene coating on Cu decreases Cu dissolution. The results are in line with the results reported by Stankovic et al. [85]. In that study, they revealed that the shift in the polarization curve indicates that the graphene coating is a corrosion barrier for the Cu substrate. Also, polarization resistance increased for the graphene-coated Cu compared to bare Cu indicating that graphene coating acts as a barrier to the Cu substrate and consequently reducing the Cu corrosion. Figure 4-17 displays the Tafel polarization curves of the Cu and Cu coated samples with HVOF. As can be seen the Cu coated sample is shifted about 50 mV more positive compared with the bare Cu. Superhydrophobic coatings produced by HVOF also showed improvement in corrosion stability. These results can be compared with a recent experiment conducted by Kumari et al. [86] that corrosion resistance is enhanced by

nanostructured graphene-polymer composite coating on copper. Their founding showed that corrosion inhibition efficiency (η) improved by 95.4%.

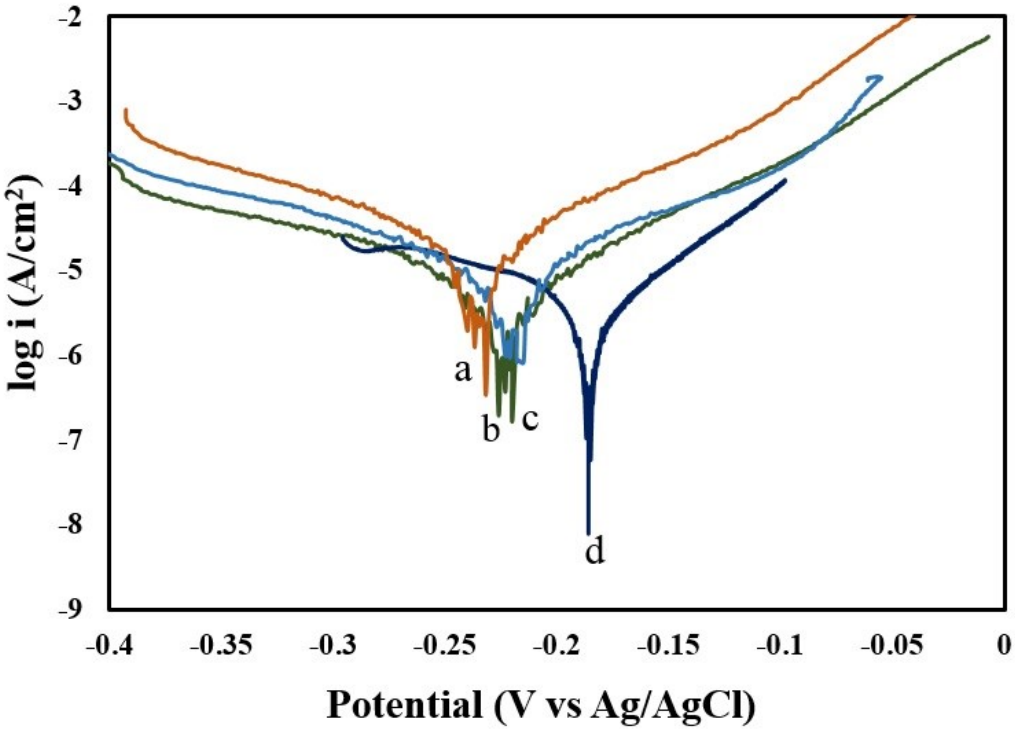

Figure 4-17. Tafel polarization curves of a) Bare Cu, b) Cu-S, and c) Cu -LR-HVOF-S, and d) Cu-GNP-LR-HVOF-S

Table 4-3 summarizes the information about the values of corrosion potential, corrosion current density (I_{corr}) and corrosion rate (CR) of bare Cu and Cu-GNP-coated Cu with HVOF and APS processes. The intersection of linear portions of the anodic and cathodic curves determines the current density of Cu-GNP coated samples and are shown to be lower than the ones of bare copper. The decrease in the current density of Cu-GNP coated Cu suggests that the coating is corrosion resistance. It can be attributed to the presence of graphene nanoplatelets that protect the electron and ion transportation between the Cu substrate and NaCl solution.

Table 4-3. Summary of the values of E_{corr}, I_{corr} and CR for the bare Cu and Cu-GNP-coated Cu

Sample	E_{corr} (mV)	I_{corr} (μA/cm^2)	CR (mm/year)
Bare Cu	-230	31.5	0.36
Cu-GNP-MP-APS-S	-185	6.30	0.06
Cu-GNP-LR-HVOF-S	-170	3.16	0.03

The corrosion resistance efficiency (η) of Cu-GNP coated Cu by HVOF is calculated using equation (4.6) [87]

$$\eta = \frac{[I_{Cu} - I_{Cu/GNP}]}{I_{Cu}} \times 100 \qquad \text{Eq. (4.6)}$$

Where (I) shows the current density. The corrosion resistance efficiency of 80 and 89% was calculated for Cu-GNP-MP-APS-S and Cu-GNP-LR-HVOF-S samples, respectively.

Also, the corrosion rate (CR) is calculated using equation (4.7) based on ASTM standard G102 [87].

$$CR = k\left[\frac{I_{corr}}{\rho A}\right] \times EW \qquad \text{Eq. (4.7)}$$

Where (k) is a constant that defines the units for the corrosion rate , and the value is 3272 mm/year, ρ is the density of Cu and is equal to 8.94 g/cm^3, (A) represents an area of the samples (1 cm^2), and EW is the equivalent weight of Cu which is equal to 31.7 g. The CR of bare Cu and Cu-GNP-LR-HVOF-S is calculated to be 0.36 and 0.03 mm/year, respectively. The result shows that the Cu-GNP coating with HVOF on the substrate improved the corrosion stability by approximately 12 times when compared to bare Cu. Nonetheless, the results of pure Cu coatings with HVOF were not considerably different from bare copper. This shows that the Cu-GNP coating with HVOF protects Cu from corrosion.

In Figure 4-18, the Tafel polarization curves of the Cu and Cu coated samples with HVOF and APS are presented in order to compare the effect of different coating procedure on corrosion results. The HVOF coated sample shows the lowest value of I_{corr} and the most positive amount of

corrosion potential (E_{corr}). Since the temperature in HVOF is lower than that of the APS process, it can be concluded that more graphene nanoplatelets were maintained in the HVOF process and had an effective contribution in corrosion stability. Akhtari et al. [88] also reported that the HVOF-sprayed samples showed greater corrosion protection than the plasma-sprayed samples. In general, the HVOF method produced more robust coats with better corrosion resistance compared to the plasma coating method. It is worth mentioning in the corrosion rate calculations of the current work the projected surface area was considered without taking into account the supplementary surface due to the roughness of the coating surfaces. So, the results with considering the real surface including the roughness would result in even lower I_{corr} due to the larger surface of the coatings.

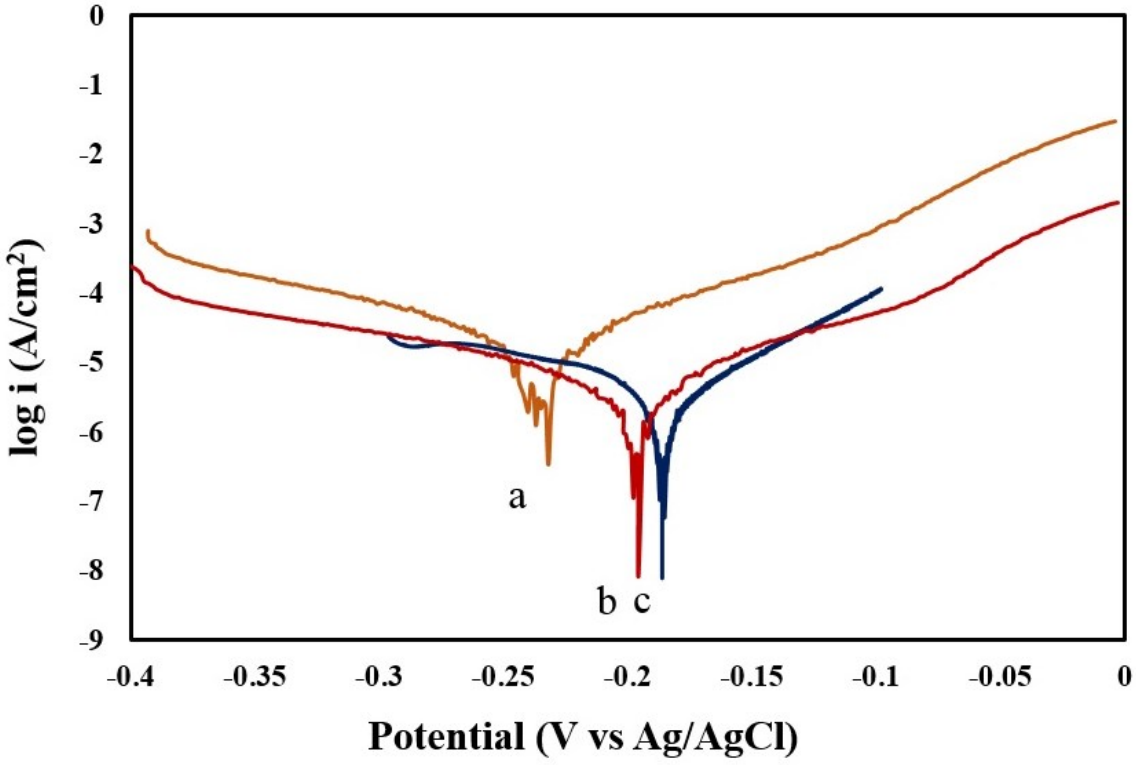

Figure 4-18. Tafel polarization curves of a) Bare Cu, b) Cu-GNP-MP-APS-S and c) Cu-GNP-LR-HVOF-S

Chapter 5. Conclusions and Future Work

Experimental research was performed to develop a Cu-GNP micro-textured coating to promote dropwise condensation through optimization of the coating procedures. To investigate the effect of the addition of a graphene nanoplatelets on the microstructure and stability of the coating, several samples with two different thermal spraying methods (APS and HVOF) and parameters were developed. The spraying strategy used was to minimize the operational temperature of the process to maintain graphene nanoplatelets properties. The first set of samples was sprayed with copper as a feedstock to determine the window of operation in the APS process. The hydrogen flow rate was the variable parameter to optimize the process; consequently, the plasma power was chosen accordingly. After finding the lowest temperature to form a coating, GNP was added to the feedstock to determine its impact on the microstructure and properties of the final coating. To reduce the surface energy, samples were treated by a stearic acid solution. The second set was sprayed with the HVOF process using the same strategy to optimize the process for maintaining the GNP in the coatings and developing further desired microstructures.

The hydrophobicity of the Cu-GNP coatings improved and water contact angle values of 152° and 162° were achieved by optimizing the APS and HVOF processes respectively. Regarding mobility, the HVOF Cu-GNP coated samples showed a better sliding angle of less than 1°. The superhydrophobicity is a complex phenomenon that includes surface energy and micro-structured morphology as contributing factors. Cu-GNP coatings have a surface morphology that can promote non-wetting behaviour by controlling the deposition parameters. The intrinsic hydrophobic properties of graphene are an asset to develop the desired surface chemistry.

The image analyses of the APS coatings showed a lamellar structure containing some flower shape features that are assumed to encourage the non-wetting trend. The HVOF coating showed more homogenous as well as denser morphology. With optimizing the parameters, GNP embedded in the Cu matrix was observable. Raman analysis further demonstrates the presence of

GNP in the coating while the defects in its structure increased after thermal spray processing. This GNP degradation is larger in APS coatings as compared to HVOF ones. Further characterization to assess corrosion and chemical stability showed Cu-GNP HVOF coating improves the corrosion stability and makes it more suitable for long-term condensing applications. With these observations, it can be concluded that, for this work, the GNP could be preserved in the coating process and HVOF is a better method to deposit Cu-GNP coatings because of denser coating that can maintain the thermal conductivity compared to APS for potential future applications in heat transfer.

Additionally, GNP seems to be helpful to add different levels of roughness encouraging the desired morphology. Also due to its natural hydrophobicity, it can improve dropwise condensation. Finally, GNP has a useful role in improving the corrosion stability of the coating.

For future work, condensation test is highly recommended to evaluate the efficiency of the coating. Also, cold spray would be another method of interest to spray Cu-GNP. Due to the lower temperature, the limitations during the coating process would decrease. Furthermore, another experimental work would be using tubular-shaped substrates as the actual application in heat transfer requires the coating on such a substrate where its curvatures may have an additional effect on the microstructure of the coating.

Additionally, the investigation of other mechanical properties like wear resistance and durability of the coating can be considered valuable for industrial applications. Thermal conductivity of the coating is also very important to be evaluated.

References

[1] D. J. Preston, D. L. Mafra, N. Miljkovic, J. Kong, and E. N. Wang, "Scalable Graphene Coatings for Enhanced Condensation Heat Transfer," *Nano Lett.*, vol. 15, no. 5, pp. 2902–2909, May 2015.

[2] G.-T. Kim, S.-J. Gim, S.-M. Cho, N. Koratkar, and I.-K. Oh, "Wetting-Transparent Graphene Films for Hydrophobic Water-Harvesting Surfaces," *Adv. Mater.*, vol. 26, no. 30, pp. 5166–5172, Aug. 2014.

[3] E. Mansfield, J. W. Sowards, and W. J. Crookes-goodson, "Findings and Recommendations from the NIST Workshop on Alternative Fuels and Materials: Biocorrosion," *J. Res. Natl. Inst. Stand. Technol.*, vol. 120, pp. 28–36, 2015.

[4] D. Attinger *et al.*, "Surface engineering for phase change heat transfer: A review," *MRS Energy Sustain.*, vol. 1, p. E4, Nov. 2014.

[5] S. M. Tong Y, Bohmb S, "Graphene based materials and their composites as coatings," *Austin J Nanomed Nanotechnol*, vol. 1, no. 1, pp. 1–16, 2013.

[6] X. Chen, R. S. Patel, J. A. Weibel, and S. V. Garimella, "Coalescence-Induced Jumping of Multiple Condensate Droplets on Hierarchical Superhydrophobic Surfaces," *Sci. Rep.*, vol. 6, no. 1, p. 18649, May 2016.

[7] N. Sharifi, F. Ben Ettouil, M. Mousavi, M. Pugh, C. Moreau, and A. Dolatabadi, "Superhydrophoibcity and Water Repelling Characteristics of Thermally Sprayed Coatings," in *International Thermal Spray Conference and Exposition (ITSC)*, 2013.

[8] A. Bejan and A. D. Kraus, *Heat transfer handbook*. J. Wiley, 2003.

[9] J. W. Rose, "Dropwise condensation theory and experiment: A review," *Proc. Inst. Mech. Eng. Part A J. Power Energy*, vol. 216, no. 2, pp. 115–128, Jan. 2002.

[10] N. Sharifi, M. Pugh, C. Moreau, and A. Dolatabadi, "Developing hydrophobic and superhydrophobic TiO2 coatings by plasma spraying," *Surf. Coatings Technol.*, vol. 289, pp. 29–36, Mar. 2016.

[11] R. Tadmor†, "Line Energy and the Relation between Advancing, Receding, and Young Contact Angles," 2004.

[12] A. Bisetto, D. Torresin, M. K. Tiwari, D. Del Col, and D. Poulikakos, "Dropwise condensation on superhydrophobic nanostructured surfaces: Literature review and experimental analysis," in *Journal of Physics: Conference Series*, 2014, vol. 501, no. 1.

[13] N. Sharifi, M. Pugh, C. Moreau, and A. Dolatabadi, "Developing hydrophobic and superhydrophobic TiO2coatings by plasma spraying," *Surf. Coatings Technol.*, vol. 289, pp. 29–36, 2016.

[14] L. Leger and J. F. Joanny, "Non-sticking drops Related content Liquid spreading," *Reports Prog. Phys.*, vol. 68, no. 11, pp. 2495–2532, 2005.

[15] B. Bhushan, Y. C. Jung, and K. Koch, "Micro-, nano- And hierarchical structures for superhydrophobicity, self-cleaning and low adhesion," *Philos. Trans. R. Soc. A Math. Phys. Eng. Sci.*, vol. 367, no. 1894, pp. 1631–1672, 2009.

[16] C. Dietz, K. Rykaczewski, A. G. Fedorov, and Y. Joshi, "Visualization of droplet departure on a superhydrophobic surface and implications to heat transfer enhancement during dropwise condensation," *Appl. Phys. Lett.*, vol. 97, no. 3, p. 33104, 2010.

[17] R. Enright, N. Miljkovic, A. Al-Obeidi, C. V Thompson, and E. N. Wang, "Condensation

on superhydrophobic surfaces: The role of local energy barriers and structure length scale," *Langmuir*, vol. 28, no. 40, pp. 14424–14432, 2012.
[18] H. Koivuluoto, C. Stenroos, M. Kylmälahti, M. Apostol, J. Kiilakoski, and P. Vuoristo, "Anti-icing Behavior of Thermally Sprayed Polymer Coatings," *J. Therm. Spray Technol.*, vol. 26, no. 1–2, pp. 150–160, 2017.
[19] B. Bhushan, Y. C. Jung, and K. Koch, "Self-cleaning efficiency of artificial superhydrophobic surfaces," *Langmuir*, vol. 25, no. 5, pp. 3240–3248, 2009.
[20] S. S. Latthe *et al.*, "A mechanically bendable superhydrophobic steel surface with self-cleaning and corrosion-resistant properties," *J. Mater. Chem. A*, vol. 3, no. 27, pp. 14263–14271, 2015.
[21] M. Nosonovsky and B. Bhushan, "Patterned Nonadhesive surfaces: Superhydrophobicity and wetting regime transitions," *Langmuir*, vol. 24, no. 4, pp. 1525–1533, 2008.
[22] R. C. Aylagas, "Visualization of condensation over micro-structured surfaces," no. July, 2016.
[23] M. Nosonovsky and B. Bhushan, "Patterned Nonadhesive surfaces: Superhydrophobicity and wetting regime transitions," *Langmuir*, vol. 24, no. 4, pp. 1525–1533, 2008.
[24] P. Roach, N. J. Shirtcliffe, and M. I. Newton, "Progess in superhydrophobic surface development," *Soft Matter*, vol. 4, no. 2, pp. 224–240, Jan. 2008.
[25] N. Sharifi, F. Ben Ettouil, C. Moreau, A. Dolatabadi, and M. Pugh, "Engineering surface texture and hierarchical morphology of suspension plasma sprayed TiO2coatings to control wetting behavior and superhydrophobic properties," *Surf. Coatings Technol.*, vol. 329, no. May, pp. 139–148, 2017.
[26] K. S. Novoselov *et al.*, "Electric Field Effect in Atomically Thin Carbon Films," Kluwer, 2004.
[27] V. Singh, D. Joung, L. Zhai, S. Das, S. I. Khondaker, and S. Seal, "Graphene based materials: Past, present and future," vol. 56, no. 8, pp. 1178–1271, 2011.
[28] X. Gao *et al.*, "Mechanical properties and thermal conductivity of graphene reinforced copper matrix composites," *Powder Technol.*, vol. 301, pp. 601–607, 2016.
[29] D. Zhang and Z. Zhan, "Strengthening effect of graphene derivatives in copper matrix composites," *J. Alloys Compd.*, vol. 654, pp. 226–233, Jan. 2016.
[30] W. Li, D. Li, Q. Fu, and C. Pan, "Conductive enhancement of copper/graphene composites based on high-quality graphene," *RSC Adv.*, vol. 5, no. 98, pp. 80428–80433, 2015.
[31] W. Li, D. Li, Q. Fu, and C. Pan, "Conductive enhancement of copper/graphene composites based on high-quality graphene," *RSC Adv.*, vol. 5, no. 98, pp. 80428–80433, Sep. 2015.
[32] S. Kumari, A. Panigrahi, S. K. Singh, and S. K. Pradhan, "Enhanced corrosion resistance and mechanical properties of nanostructured graphene-polymer composite coating on copper by electrophoretic deposition," *J. Coatings Technol. Res.*, vol. 15, no. 3, pp. 583–592, 2018.
[33] D. Berman, A. Erdemir, and A. V. Sumant, "Few layer graphene to reduce wear and friction on sliding steel surfaces," *Carbon N. Y.*, vol. 54, pp. 454–459, Apr. 2013.
[34] L. B. Boinovich and A. M. Emelyanenko, "Hydrophobic materials and coatings: principles of design, properties and applications," *Russ. Chem. Rev.*, vol. 77, no. 7, pp. 583–600, 2008.
[35] O. Leenaerts, B. Partoens, and F. M. Peeters, "Water on graphene: Hydrophobicity and

dipole moment using density functional theory," *Phys. Rev. B - Condens. Matter Mater. Phys.*, vol. 79, no. 23, pp. 1–5, 2009.
[36] X. Zhang, S. Wan, J. Pu, L. Wang, and X. Liu, "Highly hydrophobic and adhesive performance of graphene films," *J. Mater. Chem.*, vol. 21, no. 33, pp. 12251–12258, 2011.
[37] A. Akaishi, T. Yonemaru, and J. Nakamura, "Formation of Water Layers on Graphene Surfaces," *ACS Omega*, vol. 2, no. 5, pp. 2184–2190, 2017.
[38] Z. Li *et al.*, "Effect of airborne contaminants on the wettability of supported graphene and graphite," *Nat. Mater.*, vol. 12, no. 10, pp. 925–931, Oct. 2013.
[39] C. Te Hsieh and W. Y. Chen, "Water/oil repellency and work of adhesion of liquid droplets on graphene oxide and graphene surfaces," *Surf. Coatings Technol.*, vol. 205, no. 19, pp. 4554–4561, 2011.
[40] T. Forati, M. Atai, A. M. Rashidi, M. Imani, and A. Behnamghader, "Physical and mechanical properties of graphene oxide/polyethersulfone nanocomposites," *Polym. Adv. Technol.*, vol. 25, no. 3, pp. 322–328, Mar. 2014.
[41] T. Wang, Y. Zheng, A.-R. O. Raji, Y. Li, W. K. A. Sikkema, and J. M. Tour, "Passive Anti-Icing and Active Deicing Films," *ACS Appl. Mater. Interfaces*, vol. 8, no. 22, pp. 14169–14173, Jun. 2016.
[42] M. J. Nine, M. A. Cole, L. Johnson, D. N. H. Tran, and D. Losic, "Robust Superhydrophobic Graphene-Based Composite Coatings with Self-Cleaning and Corrosion Barrier Properties," *ACS Appl. Mater. Interfaces*, vol. 7, no. 51, pp. 28482–28493, Dec. 2015.
[43] D. D. Nguyen, N.-H. Tai, S.-B. Lee, and W.-S. Kuo, "Superhydrophobic and superoleophilic properties of graphene-based sponges fabricated using a facile dip coating method," *Energy Environ. Sci.*, vol. 5, no. 7, p. 7908, Jun. 2012.
[44] X. Zhang, D. Liu, Y. Ma, J. Nie, and G. Sui, "Super-hydrophobic graphene coated polyurethane (GN@PU) sponge with great oil-water separation performance," *Appl. Surf. Sci.*, vol. 422, pp. 116–124, 2017.
[45] R. K. Singh Raman *et al.*, "Protecting copper from electrochemical degradation by graphene coating," *Carbon N. Y.*, vol. 50, no. 11, pp. 4040–4045, Sep. 2012.
[46] A. S. Sai Pavan and S. R. Ramanan, "A study on corrosion resistant graphene films on low alloy steel," *Appl. Nanosci.*, vol. 6, no. 8, pp. 1175–1181, 2016.
[47] L. E. Scriven, "Physics and Applications of DIP Coating and Spin Coating," *MRS Proc.*, vol. 121, p. 717, Jan. 1988.
[48] M. Manca, A. Cannavale, L. De Marco, A. S. Aricò, R. Cingolani, and G. Gigli, "Durable superhydrophobic and antireflective surfaces by trimethylsilanized silica nanoparticles-based sol-gel processing," *Langmuir*, vol. 25, no. 11, pp. 6357–6362, 2009.
[49] K. Choy, "Chemical vapour deposition of coatings," *Prog. Mater. Sci.*, vol. 48, no. 2, pp. 57–170, 2003.
[50] A. Hozumi and O. Takai, "Preparation of ultra water-repellent films by microwave plasma-enhanced CVD," *Thin Solid Films*, vol. 303, no. 1–2, pp. 222–225, 1997.
[51] L. Wang, S. Guo, X. Hu, and S. Dong, "Facile electrochemical approach to fabricate hierarchical flowerlike gold microstructures: Electrodeposited superhydrophobic surface," *Electrochem. commun.*, vol. 10, no. 1, pp. 95–99, 2008.
[52] V. H. Pham *et al.*, "Fast and simple fabrication of a large transparent chemically-converted graphene film by spray-coating," *Carbon N. Y.*, vol. 48, no. 7, pp. 1945–1951, 2010.

[53] J.R. Davis, “Handbook of Thermal Spray Technology - Google Books,” *ASM International*, 2004. [Online]. Available: https://books.google.ca/books?hl=en&lr=&id=S0PryYc9T70C&oi=fnd&pg=PA3&dq=J.R.+Davis,+Handbook+of+thermal+spray+technology,+ASM+international2004.&ots=m70YXVYsCp&sig=6Dlqqau1h47YJQQl5h2lvtgkXAw#v=onepage&q&f=false. [Accessed: 10-Oct-2018].
[54] P. Fauchais, “Understanding plasma spraying,” *Journal of Physics D: Applied Physics*, vol. 37, no. 9. pp. 1–17, 2004.
[55] Thermal Spray Society, “Thermal Spray Technology White Paper Prepared by the Thermal Spray Society Affiliate of ASM International Mission The Value of Thermal Spray Technology What is Thermal Spray ? How It Works,” *ASM Handbood*, no. ASM Int., pp. 1–9.
[56] E. Pfender, “Fundamental studies associated with the plasma spray process,” *Surf. Coatings Technol.*, vol. 34, no. 1, pp. 1–14, 1988.
[57] P. Fauchais, M. Vardelle, and A. Vardelle, “Reliability of plasma-sprayed coatings: Monitoring the plasma spray process and improving the quality of coatings,” *J. Phys. D. Appl. Phys.*, vol. 46, no. 22, pp. 1–17, 2013.
[58] M. Oksa, E. Turunen, T. Suhonen, T. Varis, and S.-P. Hannula, “Optimization and Characterization of High Velocity Oxy-fuel Sprayed Coatings: Techniques, Materials, and Applications,” *Coatings*, vol. 1, no. 2, pp. 17–52, 2011.
[59] M. Salmanzadeh, M. Jalali Azizpour, and H. Mohammadi Majd, “Evaluation of the Effect of Spray Distance on Fracture Toughness of Thermally Sprayed Coatings,” *J. Appl. Sci.*, vol. 15, no. 4, pp. 709–714, 2015.
[60] Y. Liu, Z. Dang, Y. Wang, J. Huang, and H. Li, “Hydroxyapatite/graphene-nanosheet composite coatings deposited by vacuum cold spraying for biomedical applications: Inherited nanostructures and enhanced properties,” *Carbon N. Y.*, vol. 67, pp. 250–259, 2014.
[61] D. Ward *et al.*, “Functional NiAl-graphene oxide composite as a model coating for aerospace component repair,” *Carbon N. Y.*, vol. 105, pp. 529–543, Aug. 2016.
[62] H. Li *et al.*, “Microstructure and wear behavior of graphene nanosheets-reinforced zirconia coating,” *Ceram. Int.*, vol. 40, no. 8 PART B, pp. 12821–12829, 2014.
[63] J. W. Murray, G. A. Rance, F. Xu, and T. Hussain, “Alumina-graphene nanocomposite coatings fabricated by suspension high velocity oxy-fuel thermal spraying for ultra-low-wear,” *J. Eur. Ceram. Soc.*, vol. 38, no. 4, pp. 1819–1828, Apr. 2017.
[64] Y. Xie, H. Li, C. Zhang, X. Gu, X. Zheng, and L. Huang, “Graphene-reinforced calcium silicate coatings for load-bearing implants,” *Biomed. Mater.*, vol. 9, no. 2, p. 025009, Feb. 2014.
[65] Y. Xie, H. Li, C. Ding, X. Zheng, and K. Li, “Effects of graphene plates’ adoption on the microstructure, mechanical properties, and in vivo biocompatibility of calcium silicate coating,” *Int. J. Nanomedicine*, vol. 10, pp. 3855–3863, Jun. 2015.
[66] C. F. Glover, C. A. J. Richards, G. Williams, and H. N. McMurray, “Evaluation of multi-layered graphene nano-platelet composite coatings for corrosion control part II – Cathodic delamination kinetics,” *Corros. Sci.*, vol. 136, pp. 304–310, May 2018.
[67] S. Dardona, J. Hoey, Y. She, and W. R. Schmidt, “Direct write of copper-graphene composite using micro-cold spray,” *AIP Adv.*, vol. 6, no. 8, p. 085013, Aug. 2016.
[68] A. C. Ferrari, “Raman spectroscopy of graphene and graphite: Disorder, electron–phonon

coupling, doping and nonadiabatic effects," *Solid State Commun.*, vol. 143, no. 1–2, pp. 47–57, Jul. 2007.
[69] D. Ward, "Graphene Oxide Reinforcement in Plasma Sprayed Nickel-5%Aluminum Coatings," 2014.
[70] A. F. Stalder, T. Melchior, M. Müller, D. Sage, T. Blu, and M. Unser, "Low-bond axisymmetric drop shape analysis for surface tension and contact angle measurements of sessile drops," *Colloids Surfaces A Physicochem. Eng. Asp.*, vol. 364, no. 1–3, pp. 72–81, 2010.
[71] P. R. Waghmare and S. K. Mitra, "Contact Angle Hysteresis of Microbead Suspensions," *Langmuir*, vol. 26, no. 22, pp. 17082–17089, Nov. 2010.
[72] Y. Wan, M. Chen, W. Liu, X. X. Shen, Y. Min, and Q. Xu, "The research on preparation of superhydrophobic surfaces of pure copper by hydrothermal method and its corrosion resistance," *Electrochim. Acta*, vol. 270, pp. 310–318, Apr. 2018.
[73] L. Wang, H. Choi, J. M. Myoung, and W. Lee, "Mechanical alloying of multi-walled carbon nanotubes and aluminium powders for the preparation of carbon/metal composites," *Carbon N. Y.*, vol. 47, no. 15, pp. 3427–3433, Dec. 2009.
[74] S. J. Han, H. Il Lee, H. M. Jeong, B. K. Kim, A. V Raghu, and K. R. Reddy, "Graphene modified lipophilically by stearic acid and its composite with low density polyethylene," *J. Macromol. Sci. Part B Phys.*, vol. 53, no. 7, pp. 1193–1204, 2014.
[75] R. Abbas, N. Elkhoshkhany, A. Hefnawy, S. Ebrahim, and A. Rahal, "High Stability Performance of Superhydrophobic Modified Fluorinated Graphene Films on Copper Alloy Substrates," *Adv. Mater. Sci. Eng.*, vol. 2017, pp. 1–8, Feb. 2017.
[76] S. Vignesh, K. Shanmugam, V. Balasubramanian, and K. Sridhar, "Identifying the optimal HVOF spray parameters to attain minimum porosity and maximum hardness in iron based amorphous metallic coatings," *Def. Technol.*, vol. 13, no. 2, pp. 101–110, Apr. 2017.
[77] H. Lee, S. J. Han, R. Chidambaram Seshadri, and S. Sampath, "Thermoelectric properties of in-situ plasma spray synthesized sub-stoichiometry TiO2-x," *Sci. Rep.*, vol. 6, no. 1, p. 36581, Dec. 2016.
[78] K. Kang, H. Park, J. Kim, and C. Lee, "Role of spray processes on microstructural evolution, and physical and mechanical properties of multi-walled carbon nanotube reinforced cu composite coatings," *Appl. Surf. Sci.*, vol. 356, pp. 1039–1051, Nov. 2015.
[79] S. Kuroda, K. Isoyama, J. Kawakita, S. Kuroda, and H. Yumoto, "Key Factors for Dense Copper Coating by HVOF Spraying The development of new anti-corrosion coatings for AZ-91E magnesium alloy used for aircraft engine and gear components View project Key Factors for Dense Copper Coating by HVOF Spraying," in *ASM International*, 2003, pp. 755–762.
[80] P. Fauchais, J. R. Heberlein, and M. Boulos, "Fundamentals of Combustion and Thermal Plasma," in *Thermal Spray Fundamentals*, Boston, MA: Springer US, 2014, pp. 73–112.
[81] F. Gärtner, T. Stoltenhoff, J. Voyer, H. Kreye, S. Riekehr, and M. Koçak, "Mechanical properties of cold-sprayed and thermally sprayed copper coatings," *Surf. Coatings Technol.*, vol. 200, no. 24, pp. 6770–6782, Apr. 2006.
[82] M. S. Dresselhaus, A. Jorio, M. Hofmann, G. Dresselhaus, and R. Saito, "Perspectives on carbon nanotubes and graphene Raman spectroscopy," *Nano Letters*, vol. 10, no. 3. pp. 751–758, 2010.
[83] H. Yue *et al.*, "Effect of ball-milling and graphene contents on the mechanical properties and fracture mechanisms of graphene nanosheets reinforced copper matrix composites," *J.*

Alloys Compd., vol. 691, pp. 755–762, Jan. 2017.
[84] K. Chu and C. Jia, "Enhanced strength in bulk graphene-copper composites," *Phys. status solidi*, vol. 211, no. 1, pp. 184–190, Jan. 2014.
[85] V. Mišković-Stanković, I. Jevremović, I. Jung, and K. Rhee, "Electrochemical study of corrosion behavior of graphene coatings on copper and aluminum in a chloride solution," *Carbon N. Y.*, vol. 75, pp. 335–344, Aug. 2014.
[86] S. Kumari, A. Panigrahi, S. K. Singh, and S. K. Pradhan, "Enhanced corrosion resistance and mechanical properties of nanostructured graphene-polymer composite coating on copper by electrophoretic deposition," *J. Coatings Technol. Res.*, vol. 15, no. 3, pp. 583–592, 2018.
[87] D. Prasai, J. C. Tuberquia, R. R. Harl, G. K. Jennings, and K. I. Bolotin, "Graphene: Corrosion-inhibiting coating," *ACS Nano*, vol. 6, no. 2, pp. 1102–1108, 2012.
[88] M. A. Zavareh, E. Doustmohammadi, A. A. D. . Sarhan, R. Karimzadeh, P. Moozarm Nia, and R. S. Al/Kulpid Singh, "Comparative study on the corrosion and wear behavior of plasma-sprayed vs. high velocity oxygen fuel-sprayed Al8Si20BN ceramic coatings," *Ceram. Int.*, vol. 44, no. 11, pp. 12180–12193, Aug. 2018.